Influence of the surface roughness on inner–outer interactions in a turbulent Couette–Poiseuille flow

Cite as: Phys. Fluids **33**, 045113 (2021); https://doi.org/10.1063/5.0043043
Submitted: 06 January 2021 . Accepted: 09 March 2021 . Published Online: 08 April 2021

Jeong Hyun Kim (김정현), **Young Mo Lee** (이영모), **Jae Hwa Lee** (이재화), and **Jooha Kim** (김주하)

Physics of Fluids ARTICLE scitation.org/journal/phf

Influence of the surface roughness on inner–outer interactions in a turbulent Couette–Poiseuille flow

Cite as: Phys. Fluids **33**, 045113 (2021); doi: 10.1063/5.0043043
Submitted: 6 January 2021 · Accepted: 9 March 2021 ·
Published Online: 8 April 2021

View Online Export Citation CrossMark

Jeong Hyun Kim (김정현), Young Mo Lee (이영모), Jae Hwa Lee (이재화),[a] and Jooha Kim (김주하)[a]

AFFILIATIONS

Department of Mechanical Engineering, UNIST, 50 UNIST-gil, Eonyang-eup, Ulsan 44919, South Korea

[a]**Authors to whom correspondence should be addressed:** jhlee06@unist.ac.kr **Tel.:** 82-52-217-2350 and kimjooha@unist.ac.kr **Tel.:** 82-52-217-2362

ABSTRACT

When rod surface roughness is introduced in a turbulent Couette–Poiseuille flow (CP-flow), it is known that the Reynolds stresses near the centerline decrease due to weakened very-large-scale motions (VLSMs) and roll-cell motions [Lee, Y. M. *et al.*, "Direct numerical simulation of a turbulent Couette–Poiseuille flow with a rod-roughened wall," Phys. Fluids **30**, 105101 (2018)]. In the present study, we examine the origin of the weakened turbulent structures near the centerline in a CP-flow with roughness (CPR-flow) using a dataset from direct numerical simulation. The top–down and bottom–up interactions to organize a CP-flow are very similar to those found in earlier studies in turbulent channel/pipe and boundary layer flows. The circulation of roll-cells in the outer region induces the spanwise congregation of negative streamwise velocity fluctuating structures (u) near the wall, leading to a large-scale ejection into the outer region. This large-scale ejection contributes to the formation of a negative VLSM when two adjacent negative large-scale motions merge, and the VLSM induces the circulation of roll-cell motion due to the pure kinematics. A similar process for the inner–outer interactions is found for a CPR-flow. However, because the impact of the surface roughness suppresses the collective motion of negative u-structures near the surface roughness, strong congregation by roll-cells is observed to occur far from the wall, indicating that relatively few negative u-structures with low strength contribute to the formation of a large-scale ejection for the CPR-flow. The weakened large-scale ejection decreases the strength of the VLSM, resulting in weakened roll-cell motion.

I. INTRODUCTION

A. Canonical wall-bounded turbulent flows with surface roughness

Townsend's wall-similarity hypothesis states that turbulent motions outside a roughness sublayer are independent of surface roughness at a sufficiently high Reynolds number and that the interaction between the inner and outer layers is very weak (Townsend, 1976). In an effort to evaluate this hypothesis, a number of studies of turbulent boundary layers (TBLs) over rough walls have been conducted (Raupach *et al.*, 1991; Tachie *et al.*, 2003; Jiménez, 2004; Schultz and Flack, 2005; Flack *et al.*, 2007; Wu and Christensen, 2007; and Squire *et al.*, 2016). In TBLs with irregular three-dimensional (3-D) roughness, Schultz and Flack (2005) carried out experiments involving uniform sphere roughness, finding excellent agreement between the Reynolds stress profiles over the smooth and rough walls in the outer layer. In addition, experimental studies by Tachie *et al.* (2003) and Flack *et al.* (2007) using sand grain, wire mesh, and sandpaper roughness showed a collapse of the turbulent intensities between smooth and rough walls in the outer layer. However, in TBLs subjected to two-dimensional (2-D) rod roughness and 3-D cube roughness, the effects of the surface roughness have been shown to extend into the outer layer (Djenidi *et al.*, 1999; Krogstad and Antonia, 1999; Lee and Sung, 2007; Volino *et al.*, 2009; 2011; Lee *et al.*, 2011; and Ahn *et al.*, 2013). Similar to the results found in TBLs with rod roughness, previous studies in fully developed turbulent channel flows (i.e., pure Poiseuille flows) with one-sided rod roughness have shown a failure of wall-similarity in the outer layer (Leonardi *et al.*, 2003; Nagano *et al.*, 2004; and Orlandi *et al.*, 2006). This behavior stands in contrast to that demonstrated in previous studies using two-sided rough-wall turbulent channel flows (Ashrafian *et al.*, 2004; Bakken *et al.*, 2005), which found the establishment of outer-layer similarity between rough and smooth walls. The failure of wall-similarity in the outer layer for TBLs and one-sided turbulent channel flows with rod roughness has

been explained via the modification of turbulent structures due to the presence of surface roughness. Djenidi *et al.* (1999) experimentally investigated turbulent motions over transverse square cavities in TBLs, showing that ejections and sweeps are more intense over cavities than those for a smooth wall. Furthermore, Volino *et al.* (2009) compared turbulent structures over 2-D rod rough and smooth walls using experimental data, finding that the significant increase in the Reynolds stresses in the outer layer is due to large-scale turbulent motions emanating from the 2-D surface roughness.

Contrary to previous studies of canonical wall-bounded turbulent flows (i.e., TBLs and Poiseuille flows) with rod roughness, a recent direct numerical simulation (DNS) study by Lee *et al.* (2018) showed that the Reynolds stresses in a turbulent plane Couette–Poiseuille flow (CP-flow) decrease in the outer layer when rod roughness is imposed on the bottom surface. Here, a CP-flow is defined as a flow driven by both the pressure gradient and the velocity shear on the top moving wall. They reported that the decrease in the Reynolds stresses in the outer layer is attributed to the weakened very-large-scale motions (VLSMs) and the roll-cell motions near the centerline. It should be noted that in a CP-flow, very long high- and low-speed streaks in the core region are organized in the form of counter-rotating pairs of rolls, and these longest structures are responsible for the generation of a large amount of turbulent energy near the centerline, similar to features in pure turbulent Couette flows (Tsukahara *et al.*, 2006; Pirozzoli *et al.*, 2011; Avsarkisov *et al.*, 2014; Lee and Moser, 2018; Kim and Lee, 2018; and Kim *et al.*, 2020). In order to identify the origin of the reduced Reynolds stresses in the outer layer in a CP-flow due to surface roughness, it is important to study how the VLSMs and roll-cells are organized in canonical wall-bounded turbulent flows according to the literature in this area.

B. Organization of very-large-scale motions and roll-cell motions

The existence of VLSMs was first observed in the premultiplied one-dimensional (1-D) spectrum of streamwise velocity fluctuations measured by hot-wire in turbulent pipe flows (Kim and Adrian, 1999). A conceptual model of VLSMs was suggested in which hairpins align coherently in groups to form long packets, and packets align coherently to form VLSMs. In other words, VLSMs result from the streamwise concatenation of large-scale motions (LSMs). Here, the LSMs and VLSMs are defined with a streamwise length scale of 1–3h and greater than 3h, respectively, where h is the channel half-height, the pipe radius, or the boundary layer thickness with distinction. This concatenation process has been studied extensively in both experimental and numerical studies (Dennis and Nickels, 2011; Lee and Sung, 2011; Baltzer *et al.*, 2013; Lee *et al.*, 2014; and Hwang *et al.*, 2016). Lee and Sung (2011) showed that the streamwise stretching of LSMs causes the head of the upstream LSM meeting the tail of the downstream LSM in a TBL flow and concatenating by merger. In addition, Lee *et al.* (2014) reported that the convection velocity of the streamwise velocity fluctuations depends on the strength of the velocity fluctuations in a turbulent channel flow, and this difference in the convection velocity leads to concatenation between in-line low-speed LSMs. The VLSM organization mechanism has been further developed by Baltzer *et al.* (2013) and Lee *et al.* (2019), who showed using a DNS dataset of turbulent pipe flows that the concatenation of LSMs possesses dominant helix angles with an azimuthal offset to form VLSMs. Based on a proper orthogonal decomposition (POD) analysis, Baltzer *et al.* (2013) and Lee *et al.* (2019) found that the roll-cell motions centered above the log layer are created by the preferred spanwise offset of LSMs that concatenate to form VLSMs. Alternative views with regard to the organization of VLSMs in previous studies include the following: (1) VLSMs are sustained by a mechanism similar to a self-sustained process in the near-wall region (Hamilton *et al.* 1995; Hwang and Cossu, 2010) and (2) VLSMs arise from a linear amplification mechanism (del Álamo and Jiménez, 2006; McKeon and Sharma, 2010).

From a different perspective, Toh and Itano (2005) demonstrated the existence of a cosupporting cycle capable of explaining the inner–outer interactions between outer-layer VLSMs and near-wall small-scale motions by medium roll-cell motions in the outer layer of a turbulent channel flow. They showed that roll-cells in the outer region induce the gathering of near-wall small-scale motions in the spanwise direction and that congregated (or collective) small-scale motions in the near-wall region generate an influx of fluid from the near-wall region to the outer region (i.e., a large-scale eruption). The induced large-scale eruption serves to maintain the circulating pattern of a roll-cell in the outer layer. A subsequent study by Hwang *et al.* (2016) to investigate the relationship between a large-scale ejection and the streamwise concatenation process for VLSMs in a turbulent channel flow showed that a large-scale eruption or ejection by congregated small-scale motions in the near-wall region can contribute to the streamwise merging of LSMs, with these LSMs subsequently forming a VLSM. The role of the large-scale ejection in the formation of the VLSM indicates that two different approaches of the concatenation process of LSMs and cosupporting cycle are interlinked. Furthermore, based on synthetically constructed patterns of VLSMs using a hairpin packet model, Lee *et al.* (2019) showed that roll-cell patterns are pure kinematic consequences of the velocity induction within the VLSMs and that they sweep to organize near-wall small-scale motions beneath the VLSM patterns, consistent with an earlier observation by Toh and Itano (2005).

C. Objective of the present study

In the present study, we investigate the modification of the overall process of the sustenance (or formation) of VLSMs and roll-cell motions near the centerline in a CP-flow by surface roughness based on previous approaches (especially from Toh and Itano, 2005; Hwang *et al.*, 2016; and Lee *et al.*, 2019). It should of course be noted that the proposed mechanism is only one possibility. Nevertheless, this would provide solid comprehension of the generation process of VLSMs and roll-cell motions focusing on inner–outer interactions in turbulent Couette–Poiseuille flows over smooth and rough walls, as much effort in previous studies was devoted to confirming the presence of very long high- and low-speed streaks in the core region in a CP-flow with a smooth wall (Pirozzoli *et al.*, 2011). Using a dataset from the DNS of a CP-flow with a smooth wall (Lee *et al.*, 2018), we show that bottom–up and top–down interactions, similar to the cosupporting cycle in a turbulent Poiseuille flow are important for the spatial organization of VLSMs and roll-cells near the centerline. However, the dynamics related to the generation of the VLSMs and roll-cell motions, in both the inner and outer layers in a CP-flow, are influenced by the surface roughness, leading to weakened VLSMs and roll-cells with accompanying reductions of the Reynolds stresses.

TABLE I. Numerical details for DNSs of turbulent Couette–Poiseuille flows with smooth and rough walls. $Re_{\tau S}$ and $Re_{\tau M}$ denote the friction Reynolds numbers at the bottom and top walls, respectively. The subscript "0" indicates a value in a pure turbulent Poiseuille flow.

Case	$\tilde{u}_M/U_{co}$	$Re_{\tau S}$	$Re_{\tau M}$	L_x/h	L_y/h	L_z/h	N_x, N_y, N_z	Δx_0^+	Δz_0^+	$\Delta y^+_{0,\min}$
CP-flow	1.3	245	242	40π	2	6π	4097, 180, 1025	8.7	5.2	0.2
CPR-flow	1.3	630	235	40π	2	6π	4097, 180, 1025	8.7	5.2	0.2

This paper is organized as follows: A brief description of a computational approach for DNSs of turbulent Couette–Poiseuille flows over smooth and rough walls is presented in Sec. II. After the introduction of an idealized schematic of the formation process of the VLSMs and roll-cells, we investigate systematically the modification of the inner–outer interactions for the formation of the VLSMs and roll-cells by surface roughness in Sec. III. Finally, a summary of the main findings is provided in Sec. IV.

II. COMPUTATIONAL DETAILS

The governing equations in Cartesian coordinates for an incompressible, fully developed turbulent Couette–Poiseuille flow were integrated in time using the fractional step method along with the implicit velocity decoupling procedure. To describe the surface roughness in Cartesian coordinates, the immersed boundary method is used, and discrete-time momentum forcing is explicitly calculated in time to satisfy the no-slip condition on the immersed boundary. The position is denoted as $\boldsymbol{x} = (x, y, z)$, where x, y, and z denote the streamwise, wall-normal, and spanwise coordinates, respectively, with the corresponding velocity components $\tilde{\boldsymbol{u}} = (\tilde{u}, \tilde{v}, \tilde{w})$. All variables are normalized by the laminar channel centerline velocity (U_{co}) and the channel half-height (h), and the Reynolds number is defined as $Re = U_{co}h/\nu$, where ν is the kinematic viscosity. The computational domain size, mesh resolution and friction Reynolds number ($Re_\tau = U_\tau h/\nu$) are summarized in Table I, where U_τ is the local mean friction velocity on a wall. Here, CP-flow and CPR-flow indicate a Couette–Poiseuille flow with a smooth wall and a Couette–Poiseuille flow with surface roughness, respectively. The subscripts "S" and "M" indicate stationary and moving walls, respectively. Two DNSs are independently performed in a very long computational domain in the streamwise direction with a domain size of $(L_x, L_y, L_z) = (40\pi h, 2h, 6\pi h)$, which is sufficient to capture the longest structures for a CP-flow with a smooth wall. The no-slip boundary condition is adopted on the bottom wall and a constant velocity ($\tilde{u}_M/U_{co} = 1.3$) is applied at the top wall for a CP-flow, similar to previous studies of Pirozzoli *et al.* (2011) and Kim and Lee (2018). Periodic boundary conditions are employed in streamwise and spanwise directions. A nonuniform grid is used in the wall-normal direction with the hyperbolic-tangent function and a uniform grid is adopted in both the streamwise and spanwise directions.

Figure 1 shows a schematic of the computational domain of a turbulent-plane CP-flow with rod roughness. Transverse 2-D rods are periodically arranged in the streamwise direction only on the bottom wall, and the roughness height (k) is $k/h = 0.12$, similar to the configurations used in previous studies by Orlandi *et al.* (2006) and Burattini *et al.* (2008) in one-sided turbulent channel flows with rod roughness. The streamwise pitch (p) between the roughness elements is $p/k = 8$ to introduce strong inner- and outer-layer interaction with the maximum form drag (Leonardi *et al.*, 2003; Lee and Sung, 2007). Two streamwise locations (I and II) are defined to examine the effects of the streamwise variation on the turbulent statistics: I, the center of the roughness valley; and II, the center of the roughness crest. In the present study, a bracket $\langle\cdot\rangle$ and capital letters (e.g., U) denote spatially (only in the spanwise direction) and temporally averaged statistics, and a bracket with the subscript "t" $\langle\cdot\rangle_t$ indicates only temporally averaged statistics. The friction velocity (U_τ) is directly estimated from the total drag, which is the sum of the mean skin-frictional and form drags averaged on the horizontal plane (Leonardi *et al.*, 2003; Lee and Sung, 2007). As usual, the superscript + indicates normalization by the mean friction velocity on the bottom wall ($U_{\tau S}$). The velocity fluctuations (i.e., $\boldsymbol{u}$) are defined as $\boldsymbol{u} = \tilde{\boldsymbol{u}} - \langle\boldsymbol{u}\rangle$. The flow parameters for the CPR-flow are

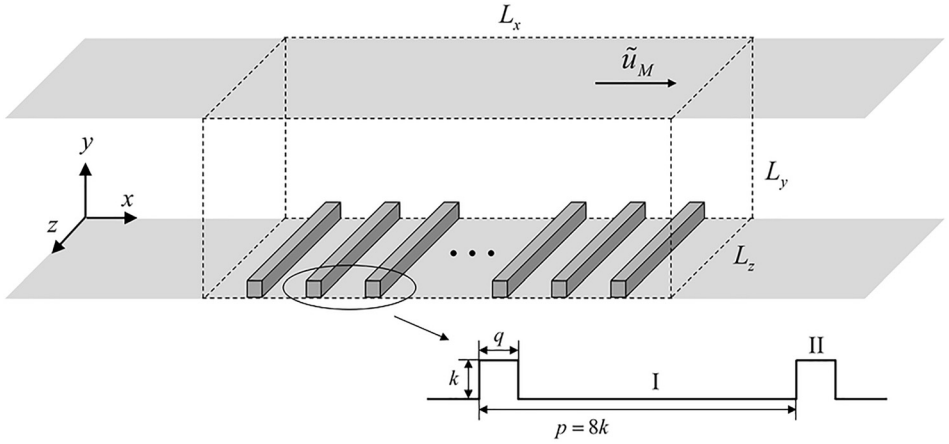

FIG. 1. Schematic of the computational domain for a turbulent Couette–Poiseuille flow with a rod-roughened wall. Surface roughness is periodically placed on the stationary bottom wall (no-slip condition). The top wall without roughness moves along the streamwise direction with $\tilde{u}_M/U_{co} = 1.3$. Two streamwise locations within a streamwise pitch ($p/k = 8$) are defined in the middle of the valley (I) and crest (II). The roughness height (k) and width ($q = k$) are identical.

TABLE II. Flow parameters for a Couette–Poiseuille flow with surface roughness. The parameter k_s indicates the sand-grain roughness height extracted using the relationship $\Delta U^+ = \frac{1}{\kappa}\ln(k_s^+) - 3.2$ (Raupach *et al.*, 1991), where ΔU^+ and κ are the roughness function and the von Kármán constant ($\kappa = 0.41$), respectively.

ΔU^+	k_s^+	k_s/h	k^+	k/h	k_s/k
12.5	456.2	0.72	75.6	0.12	6.0

summarized in Table II. Further numerical details and validation of our DNS data are found in Lee *et al.* (2018).

III. RESULTS AND DISCUSSION

A. Weakened VLSMs and roll-cell motions

Because the generation of Reynolds stresses for a CP-flow is closely associated with very long motions (or counter-rotating roll-cell motions) residing near the centerline (Pirozzoli *et al.*, 2011; Lee *et al.*, 2018), temporally averaged u-structures are analyzed, as shown in Fig. 2, to examine the origin of the Reynolds stress reduction in the outer layer for a CPR-flow compared to a CP-flow (e.g., see the inset for the reduction of the Reynolds shear stress in Fig. 2). In Figs. 2(a) and 2(b), red and blue isosurfaces indicate positive and negative u-structures, respectively. Consistent with previous experimental and numerical studies in CP-flows and pure Couette flows (Bech *et al.*, 1995; Komminaho *et al.*, 1996; Kitoh *et al.*, 2005; Tsukahara *et al.*, 2006; Pirozzoli *et al.*, 2011; Avsarkisov *et al.*, 2014; Gandía-Barberá *et al.*, 2018; and Lee and Moser, 2018), very-large-scale streaky patterns of high and low momentum throughout the domain are clearly observed for the CP-flow in Fig. 2(a). These streaky patterns near the centerline are closely associated with counter-rotating vortices (i.e., roll-cell motions), as shown in Fig. 2(c-i). The roll-cell motions induce spanwise dispersive and congregated motions near the bottom wall, and these spanwise motions are related to the positive and negative u-structures, respectively. Although very long streaky structures are also observed for the CPR-flow with similar spanwise spacing between alternating high- and low-speed streaks, the strength of the negative and positive u-structures in Figs. 2(c-ii) and 2(c-iii) is weakened irrespective of the streamwise location (locations I and II). These weakened VLSMs in the CPR-flow are interlinked with reduced roll-cell motions that are constructed using the temporally averaged v- and w-structures in Fig. 2(c).

The weakened VLSMs near the centerline are also confirmed through the energy spectra of the velocity fluctuations. The two-sided spanwise energy spectra of all velocity fluctuating components (u_i) as a function of the spanwise wavenumber (k_z) are defined as follows:

$$S_{ij}(x, y, k_z; x_r, y_r) = \frac{1}{2\pi}\int_{-\infty}^{\infty} e^{-jk_z r_z}\langle u_i(x_r, y_r, z)u_j(x, y, z + r_z)\rangle dr_z, \tag{1}$$

which is the 1-D Fourier transform of the two-point correlation with spatial homogeneity in the spanwise direction. Here, x_r and y_r correspondingly indicate the reference streamwise and wall-normal locations. When $x = x_r$ and $y = y_r$, the one-sided spanwise wavenumber (k_z) spectrum is then determined as follows:

$$\Phi_{ij}(k_z) = S_{ij}(k_z) + S_{ij}(-k_z) = 2\mathrm{Re}\{S_{ij}(k_z)\}. \tag{2}$$

Figure 3 shows premultiplied spanwise energy spectrum maps of the velocity fluctuations of CP- and CPR-flows with the wall-normal position. Here, the streamwise reference location (x_r) is fixed at $20\pi h$ (location I for the CPR-flow), although the spectrum for the CP-flow is independent of x_r. In the map of $k_z\Phi_{uu}$ for the CP-flow in Fig. 3(a), a clear secondary outer peak (white cross) of $k_z\Phi_{uu}$ is observed at the channel centerline with a spanwise wavelength of approximately $\lambda_z/h = 4.6$, corresponding to the presence of energetic VLSMs. This energy in the outer region of the CP-flow penetrates deeply into the near-wall region, and the outer energy transfer is related to the footprint of the very-large-scale structure (Mathis *et al.*, 2009; Pirozzoli *et al.*, 2011). Although a similar outer peak is also visible for the CPR-flow in Fig. 3(b), the magnitude of the outer peak is notably weakened with suppressed energy transfer into the near-wall region. Consistent with the energy distribution of $k_z\Phi_{uu}$, the premultiplied energy spectra of $k_z\Phi_{vv}$ and $k_z\Phi_{ww}$ for the CPR-flow in Figs. 3(d) and 3(f) show weakened secondary energetic outer peaks at the channel centerline with spanwise wavelengths of $\lambda_z/\delta = 4.7$–4.8 compared to those for the CP-flow in Figs. 3(c) and 3(e). Based on the spanwise energy spectra of $k_z\Phi_{vv}$ and $k_z\Phi_{ww}$ shown in Fig. 3, a spanwise cutoff wavelength of $\lambda_z/h = 4.0$ is defined (horizontal dashed lines) to separate very large scales from smaller scales, and an analysis of the low- and high-pass-filtered velocity fields is used to examine the relationship between the negative u-structures and the roll-cell motions in the latter. The energy distribution for the inner peaks in the energy spectrum maps is very similar to previous observations of a TBL flow with rod roughness (Nadeem *et al.*, 2015).

B. Top–down and bottom–up interactions

As described in the introduction, the streamwise concatenation process of LSMs to organize a typical VLSM in the outer region of a turbulent channel and boundary layer flows is directly associated with the cosupporting cycle by Toh and Itano (2005) (Hwang *et al.*, 2016). Furthermore, the generation of a roll-cell motion in the outer layer is interlinked with the VLSM organization (Lee *et al.*, 2019). The formation process of the VLSMs and roll-cell motions, which has been reported in previous studies, can be summarized using top–down and bottom–up inner- and outer-layer interactions (Fig. 4).

(i) The circulation of roll-cells induces the spanwise congregative motion of near-wall negative u-structures, thus gathering the near-wall streaks toward an area under the circulation.
(ii) This collective motion of near-wall streaks generates intense velocity fluctuations which are lifted away from the wall, creating a large-scale ejection into the outer layer.
(iii) The large-scale ejection contributes to a merging process between two adjacent LSMs to form a VLSM by differentiating convection velocities between the LSMs.

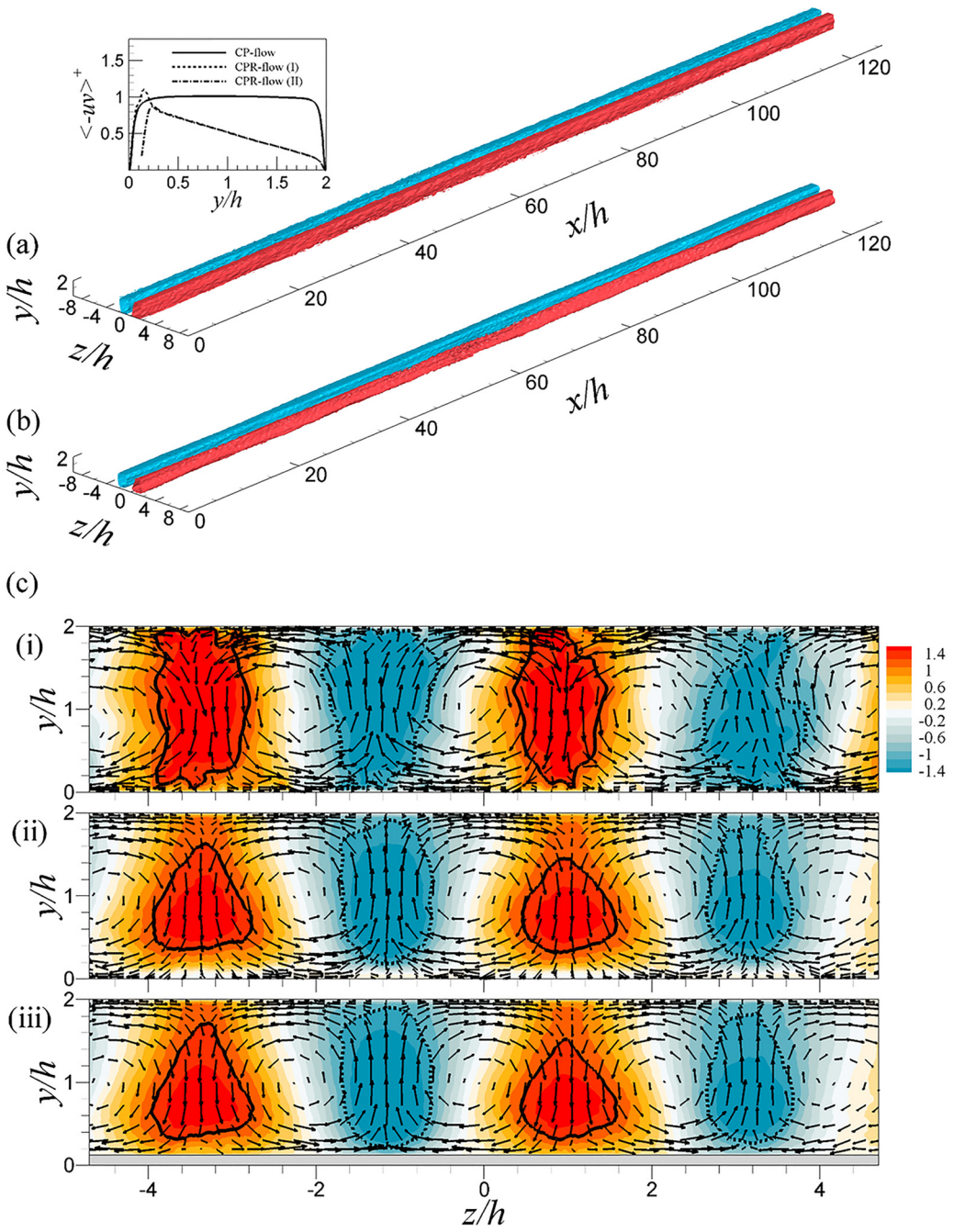

FIG. 2. [(a) and (b)] Isosurfaces of the temporally averaged u-structures ($\langle u \rangle_{\ell}/U_{\tau S}$) with the magnitude at one half of the maximum (red) and minimum (blue) values: (a) CP- and (b) CPR-flows. Two-dimensional (2-D) slices on the perspective view are shown in (c) with the in-plane vector: (i) CP-flow at $x/h = 20\pi$, (ii) CPR-flow at $x/h = 20\pi$ (location I) and (iii) CPR-flow at $x/h = 63.31$ (location II). Only part of the entire spanwise domain is depicted. In (c), line contours of $\langle u \rangle_{\ell}/U_{\tau S} = 1.2$ (solid lines) and -1.2 (dotted lines) are visible to highlight strong u-structures. The inset in the upper-left corner shows the profiles of the Reynolds shear stress in the outer coordinates for the CP- and CPR-flows.

(iv) The induced VLSM generates a roll-cell pattern by pure kinematic consequences.

In Secs. III B 1–III B 3, we will demonstrate that the generation process of VLSMs and roll-cell motions near the centerline for a CP-flow is very similar to that found in turbulent Poiseuille and boundary layer flows. The influence of the surface roughness on the process will then be scrutinized to examine the origin of the weakened VLSMs and roll-cell motions.

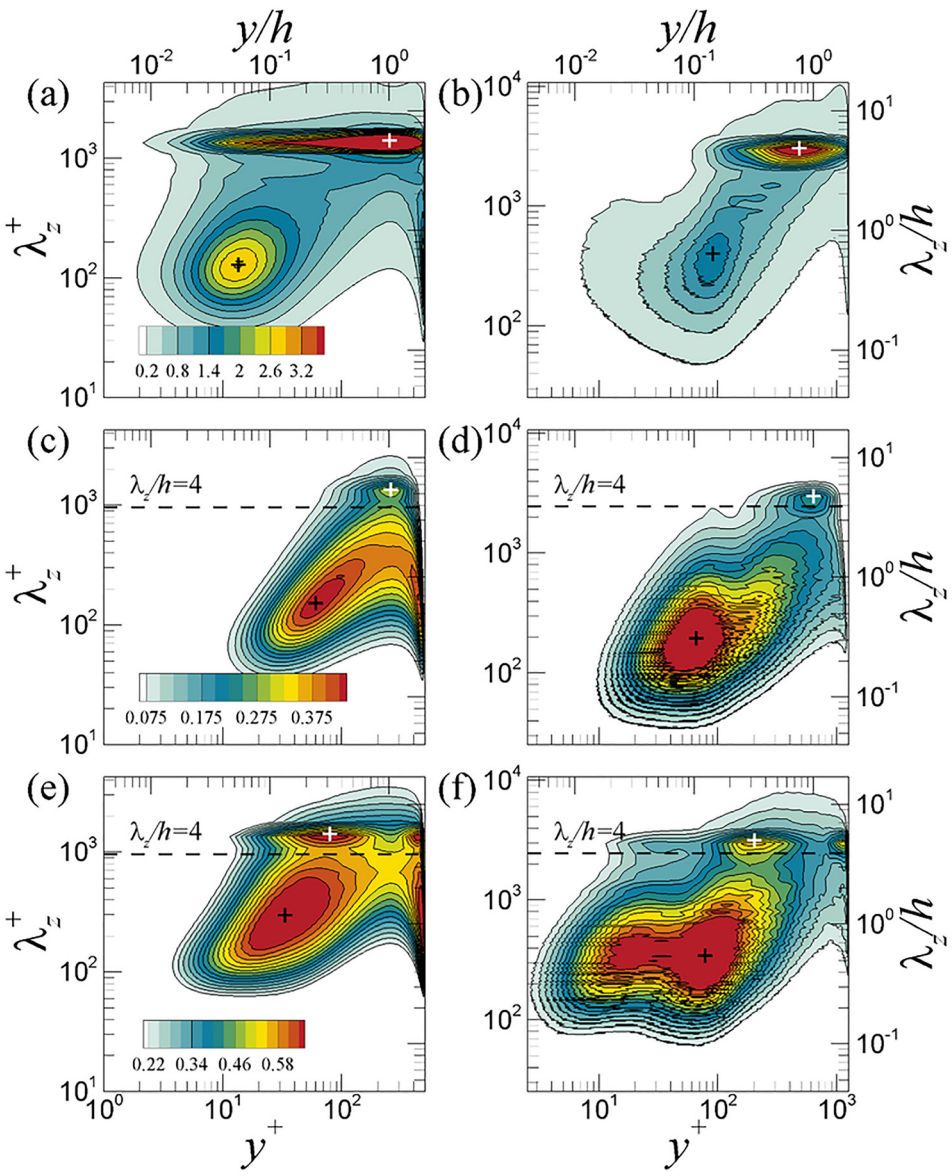

FIG. 3. Premultiplied spanwise energy spectra of the velocity fluctuations for the CP- and CPR-flows: (a) and (b) $k_z\Phi_{uu}/U_\tau S^2$, (c) and (d) $k_z\Phi_{vv}/U_\tau S^2$, and (e) and (f) $k_z\Phi_{ww}/U_\tau S^2$. Left column, CP-flow; right column, CPR-flow. In (a)–(f), the locations of the inner and outer peaks are depicted by the black and white cross symbols, respectively.

1. Spanwise congregation motion by roll-cells

The previous observation using temporally averaged structures for the CP- and CPR-flows in Sec. III A showed the presence of dispersive and congregative motions near the positive and negative VLSM patterns on the bottom wall and their association with the roll-cell patterns. Here, we will show that the spanwise congregative motion of negative u-structures on the bottom wall is induced by roll-cell motions near the centerline for CP- and CPR-flows. Because a large-scale ejection created by the congregative motions contributes to the formation of a VLSM (Hwang *et al.*, 2016), it proves convenient in this study to examine the inner and outer interactions with a focus on negative u-structures.

The collective behavior of negative u-structures is identified by the time evolution of the spanwise motion for streamwise-averaged negative u-structures, which satisfy the local minima at a given wall-normal reference height (Toh and Itano, 2005)

$$\frac{\partial u^{2D}}{\partial z}(y,z,t)=0, \quad \frac{\partial^2 u^{2D}}{\partial z^2}(y,z,t)>0, \quad u^{2D}(y,z,t)<-0.1U(y),$$

where

$$u^{2D}(y,z,t)=\frac{1}{\lambda_x}\int_0^{\lambda_x}\tilde{u}(x,y,z,t)dx, \quad \lambda_x\simeq 10h. \tag{3}$$

Here, λ_x is set to $10h$ for both flows, as this streamwise length scale is believed to be a boundary to separate VLSMs from LSMs in the core region of a CP-flow (Kim and Lee, 2018). Although the critical streamwise wavelength (λ_x) for the integral would be expected to be shorter for the CPR-flow, as discussed later, we found that changing the value of λ_x has no influence on our results (not shown here).

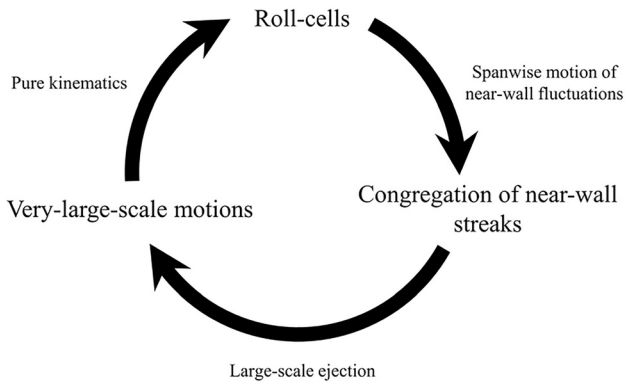

FIG. 4. Idealized process of inner–outer interactions for the formation of very-large-scale motions and roll-cell motions.

Figures 5 and 6 show the time evolution of the spanwise location of the local minima for $u^{2D}(z, t)$ in the near-wall region ($y^+ = 5$) and in the outer layer ($y/h = 0.25$ and 1.0) for the CP- and CPR-flows. The spanwise motion of negative u-structures in the near-wall region ($y^+ = 5$) in Fig. 5(a) shows the assembly of negative u-structures with time ($t^+ = tU_{\tau S}^2/\nu$) around the reference spanwise location ($z^+ = 0$), and this congregation motion for the CP-flow induces "branches" by merging, which survive for a relatively long time. Although weak branches are also observed in the vicinity of the long-term branches, they merge into the dominant branches over time. In Figs. 5(b) and 5(c), the spanwise motion of a group of local minima for the negative u-structures in the outer layer shares some similarity with that of the long-term branches in the near-wall region, consistent with the near-wall footprint of the outer-layer structure (Mathis *et al.*, 2009; Pirozzoli *et al.*, 2011). However, as the wall-normal distance from the wall increases, the congregation motion becomes less dominant. Because the spanwise scale of the negative u-structures increases away from the wall, the increased spanwise scale leads to fewer a decreased number of negative u-structures in the outer layer, resulting in less frequent collective patterns, as shown in Figs. 5(b) and 5(c).

Contrary to the observation of the CP-flow, near-wall long-term branches are hardly found for the CPR-flow in Fig. 6(a), and there are scattered patterns of negative u-structures observed. As the wall-normal reference height increases to $y/h = 0.25$ in Fig. 6(b), relatively apparent branches are shown; these branches are not related to the near-wall branches in Fig. 6(a), indicating that the near-wall spanwise motions for the CPR-flow are suppressed by the surface roughness. In Fig. 6(c) with $y/h = 1.0$, although the spanwise motions of the negative u-structures decrease, the pattern of the spanwise motions resembles that at $y/h = 0.25$ to some extent, similar to the observations for the CP-flow.

To provide a connection to the collective motions for the negative u-streaks (Figs. 5 and 6) with roll-cell motions, a conditional correlation coefficient (R) with streamwise velocity fluctuations (u) is defined as

$$R[u_{i,\,\text{roll-cells}}, u](x, y, r_z; x_r, y_r) = \frac{\langle u_{i,\,\text{roll-cells}}(x_r, y_r, z)u(x, y, z + r_z)\rangle}{\sigma_{u_i}(x_r, y_r)\sigma_u(x, y)}, \tag{4}$$

where $u_{i,\,\text{roll-cells}}$ denotes the velocity fluctuating components representing the very-large-scale circulation of roll-cells, and σ is the standard deviation. The very-large-scale circulation of roll-cells is extracted by low-pass-filtering very-large-scale wall-normal ($v_{\text{roll-cells}}$) and spanwise fluctuating motions ($w_{\text{roll-cells}}$) based on the energy spectra in Fig. 3. Because roll-cells are centered in the channel centerline for both flows (Fig. 2), the wall-normal location for the conditional correlation coefficient is set to $y_r/h = 1.0$. Although the streamwise reference location (x_r) is fixed at $20\pi h$ (location I for the CPR-flow), the correlation contours are not affected by the location.

Figure 7 shows the spatial organization of the correlation coefficients on the yz-plane ($x_r = x$) for the CP- and CPR-flows. For the

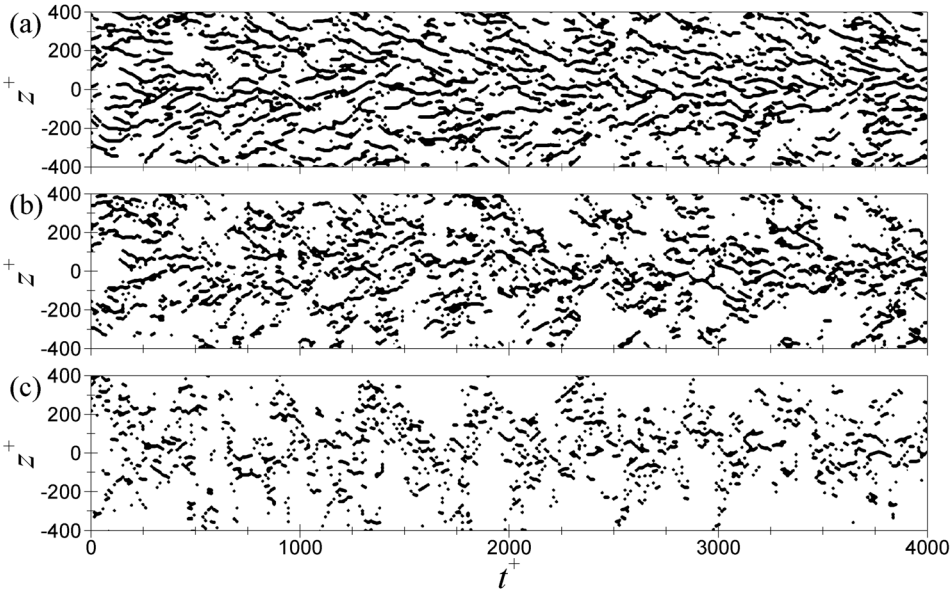

FIG. 5. Time evolution of the spanwise location for negative u-structures, which are identified as points satisfying $\partial u^{2D}/\partial z = 0$ and $\partial^2 u^{2D}/\partial z^2 > 0$ in the low-speed zone ($u^{2D} < -0.1\,U$) for the CP-flow: (a) $y^+ = 5$, (b) $y/h = 0.25$, and (c) $y/h = 1.0$.

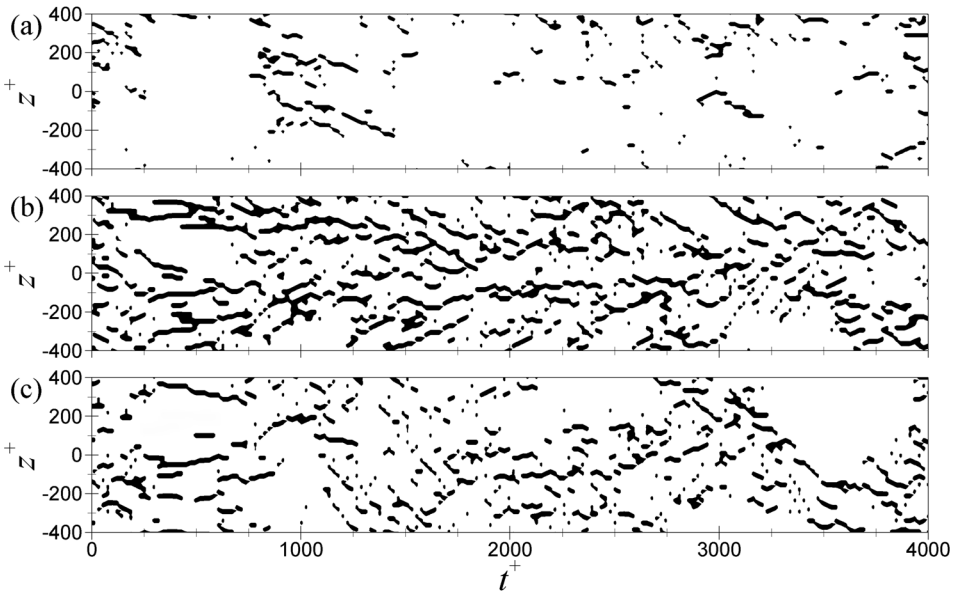

FIG. 6. Identical to those in Fig. 5, but for the CPR-flow.

CP-flow in Fig. 7(a), positive and negative contours of $R[w_{\text{roll-cells}}, u]$ beneath the centerline are found alternatively in the spanwise direction. The positive contours of $R[w_{\text{roll-cells}}, u]$ in the range of $0 < r_z/h < 2.3$ can be interpreted as motions of negative u-structures toward the negative spanwise direction. In contrast, the negative contours of $R[w_{\text{roll-cells}}, u]$ in the range of $-2.3 < r_z/h < 0$ beneath the centerline indicate motions of negative u-structures toward the positive spanwise direction, providing evidence that the spanwise component of the roll-cell motions in the channel centerline is the main source of the spanwise congregation motion of the negative u-structures on the bottom wall, most actively at $y^+ \approx 7$ ($y/h = 0.03$). The presence of opposite behavior in a region for $y/h > 1$ suggests that a roll-cell mode centered in the channel centerline generates spanwise dispersive motions of negative u-structures on the top wall. The line contours of $R[v_{\text{roll-cells}}, u]$ show negative values around the reference point at $r_z/h = 0$, and these contours of $R[v_{\text{roll-cells}}, u]$ generate a roll-cell pattern together with the contours of $R[w_{\text{roll-cells}}, u]$. The role of the counter-rotating roll-cell motions on the near-wall congregation motion in the CP-flow resembles that in an earlier observation in a turbulent channel flow (Hwang *et al.*, 2016). For the CPR-flow in Fig. 7(b), the spatial features of the correlation contours for $R[w_{\text{roll-cells}}, u]$ are similar to those for the CP-flow. However, the magnitude of the correlation peaks for $R[w_{\text{roll-cells}}, u]$ decreases, and the correlation peak for $R[w_{\text{roll-cells}}, u]$ is found in the outer region (i.e., $y/h = 0.25$), consistent with our observation in Fig. 6. The weak congregation motion with the peak in the outer region for the CPR-flow leads to the weakening of a large-scale ejection, as evidenced by the line contours for $R[v_{\text{roll-cells}}, u]$ in Fig. 7(b). The peaks of $R[w_{\text{roll-cells}}, u]$ for the CP- and CPR-flows are observed at $r_z/h = \pm 1.07$, and these locations are consistent with the spanwise spacing between the centers of the positive- and negative-VLSMs in Fig. 2(c).

2. Formation of a VLSM

In Sec. III B 1, the top–down influence of the very-large-scale circulation of roll-cells on the congregation motions of the near-wall negative u-streaks and the bottom–up influence of the large-scale ejection toward the outer region for both flows were discussed. In this section, we will explore the spatial organization mechanism of a VLSM linked to a large-scale ejection. The works by Lee and Sung (2011) and Lee

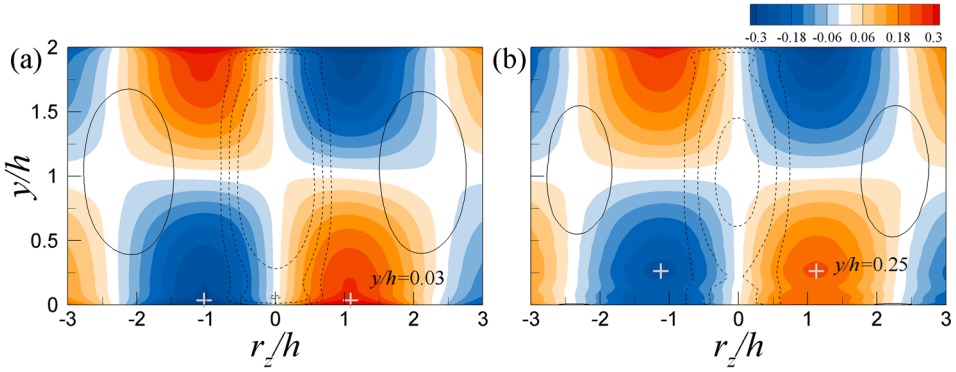

FIG. 7. Conditional two-point correlation coefficients on the yz-plane for the (a) CP- and (b) CPR-flows. The reference location in the wall-normal direction is $y_r/h = 1$. Color contours represent the correlation coefficients $R[w_{\text{roll-cells}}, u]$, and the magnitude is varied from −0.3 to 0.3 with an increment of 0.04. Line contours represent the correlation coefficients $R[v_{\text{roll-cells}}, u]$ with $R = 0.15$ (solid line) and $R = -0.2$, −0.15, and −0.1 (dashed line). White crosses denote the peak locations of $R[w_{\text{roll-cells}}, u]$ for the CP- ($y^+ \approx 7$) and CPR-flows ($y/h = 0.25$).

et al. (2014) provide the important background of the formation process of a VLSM in TBL and channel flows. The aforementioned studies found that negative u LSMs mainly undergo merging and that the merging process is facilitated by the different convection velocities between the upstream and downstream LSMs. Specifically, they showed that the convection velocities of the structures depend on their strength using the conditional correlations of negative u-structures: weak negative u-structures have a relatively high convection velocity compared to strong negative-u structures. Because the head of the upstream LSM has a high convection velocity with weak strength, the upstream structure (US) merges with the tail of the downstream LSM, which has a slow convection velocity due to a strong large-scale ejection.

The time-evolving merging process between adjacent two negative LSMs to form a VLSM for a CP-flow is depicted in Fig. 8. At $t = t_r - 14.4h/U_{co}$, two LSMs for the CP-flow have a streamwise length of approximately $10h$ and are inclined at angles of 11°–12° (see bold dashed lines). These two outer-layer structures initially have a streamwise gap of approximately $5.5h$, and they begin to merge upon the narrowing of the streamwise gap. During the merging process, the tail of the downstream structure (DS) has a slower convection speed than the head of the upstream structure (US) due to the higher magnitude of u (Lee et al., 2014). As a result, a very-long negative VLSM is formed at $t = t_r$. To show further a relationship between the streamwise concatenation process of the LSMs and a large-scale ejection, the time evolution of the near-wall horizontal flow fields (left column) near the tail of the downstream LSM during the merging process for the CP-flow is shown in Fig. 9. In addition, the cross-stream flow fields (right column) extracted from the streamwise locations, where large-scale ejection motions are dominant (see the vertical solid lines in Fig. 8), are presented. In each figure, red circles identify negative u-structures related to the congregation motions to form a large-scale ejection. In the early stage ($t = t_r - 14.4h/U_{co}$), data on both the xz- and yz-planes show five strong near-wall streaks in the range of $-0.82 \le z/h \le 0.78$ with spanwise separations (see red circles). With time, they gradually congregate in the spanwise direction with reduced spanwise gap distances and create an upward motion into the top wall, as shown on the yz-plane (at $t = t_r - 9.6h/U_{co}$). The continuous congregation of the near-wall negative u-structures near the tail of the downstream LSM pulls out the intensified near-wall structures further into the outer region, creating a large-scale ejection motion after $t = t_r - 4.8h/U_{co}$. Although large-scale features originate from motions at the near-wall small-scales in the present study, it has been also reported that near-wall motions are not necessary to form large-scale outer motions in turbulent Couette flow (Rawat et al., 2015). Using over-damped large-eddy simulations, they showed that large-scale motions are still active even when the multiple small-scale structures are quenched, indicating that large-scale motions are themselves self-sustained.

Compared to the LSMs on the xy-plane at $t = t_r - 14.4h/U_{co}$ for the CP-flow in Fig. 8(a), two LSMs in the outer layer for the CPR-flow at $t = t_r - 14.4h/U_{co}$ in Fig. 10(a) have relatively short streamwise lengths, and they are inclined at angles of 13°–14° (dashed lines). Nonetheless, these structures are streamwise-concatenated with time to form a VLSM in a process similar to that for the CP-flow. Interestingly, another LSM appears further upstream in this picture (see the dashed–dotted line at $t = t_r - 4.8h/U_{co}$), and this new LSM merges with the downstream VLSM with time (not shown here). This is another indication of the commonplace nature of mergers leading to longer structures for CPR-flows.

Figure 11 shows the time evolution of the negative u-structures on the xz- and yz-planes to identify the modification of the spanwise congregated motion by the surface roughness. Contrary to the observation in the near-wall region for the CP-flow in Fig. 9, near-wall negative u-structures ($y/h < 0.25$) on the yz-plane for the CPR-flow do not create a spanwise congregated motion, consistent with our observation in Fig. 6. The origin for the suppression of the near-wall spanwise

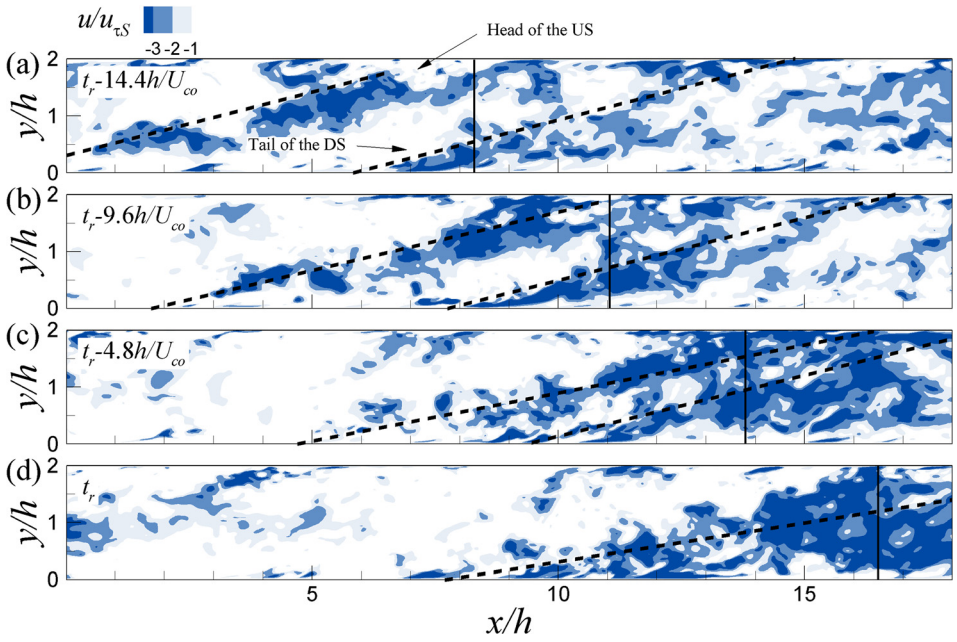

FIG. 8. Time evolution of the instantaneous negative u-structures ($u/U_{\tau S}$) for the CP-flow on the xy-plane. The LSMs are highlighted by the dashed lines. The vertical solid line in each figure indicates a streamwise location, where a large-scale ejection prevails.

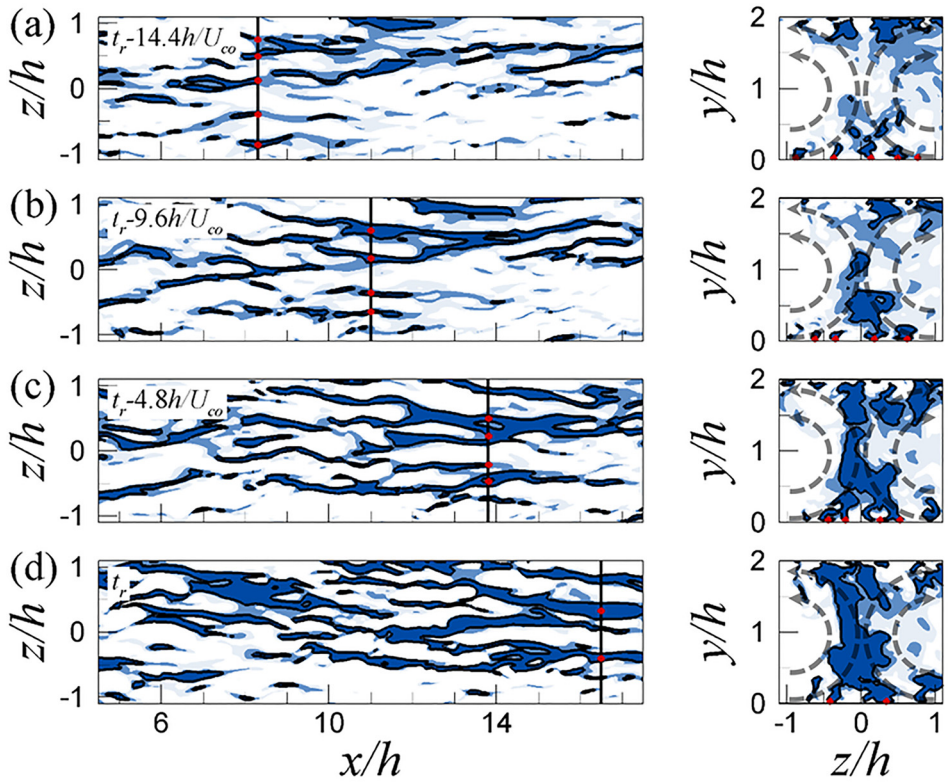

FIG. 9. Contours of the negative *u*-structures on the (left) *xz*-plane ($y^+ = 7$) and (right) *yz*-plane for the CP-flow. On the *xz*-plane, the streamwise location depicted by the straight solid line in each plot is identical to that used in Fig. 8. The flow field on the *yz*-plane is extracted at the streamwise location depicted by the solid line on the *xz*-plane, where a large-scale ejection motion prevails. For both planes, negative *u*-structures related to congregation motions are highlighted using red circles. Contour levels are identical to those in Fig. 8, and line contours indicate $u/U_{\tau S} = -3.0$ to show strong negative *u*-structures. An idealized schematic for a roll-cell motion is superimposed onto the instantaneous fields on the *yz*-plane using semicircles with the corresponding direction of rotation.

motions is not clear at this time. Instead, the outer-layer motions above $y/h = 0.25$ (see the horizontal dashed line on the *yz*-plane in Fig. 11) are most actively congregative in the spanwise direction, forming a large-scale ejection motion at $t = t_r$ despite the reduced strength (compare the colored contours on the *yz*-plane in Figs. 9 and 11). The time-evolving instantaneous view in Fig. 11 suggests that the weakened large-scale ejection for the CPR-flow compared to the CP-flow is attributable to the small number of the negative *u*-structures

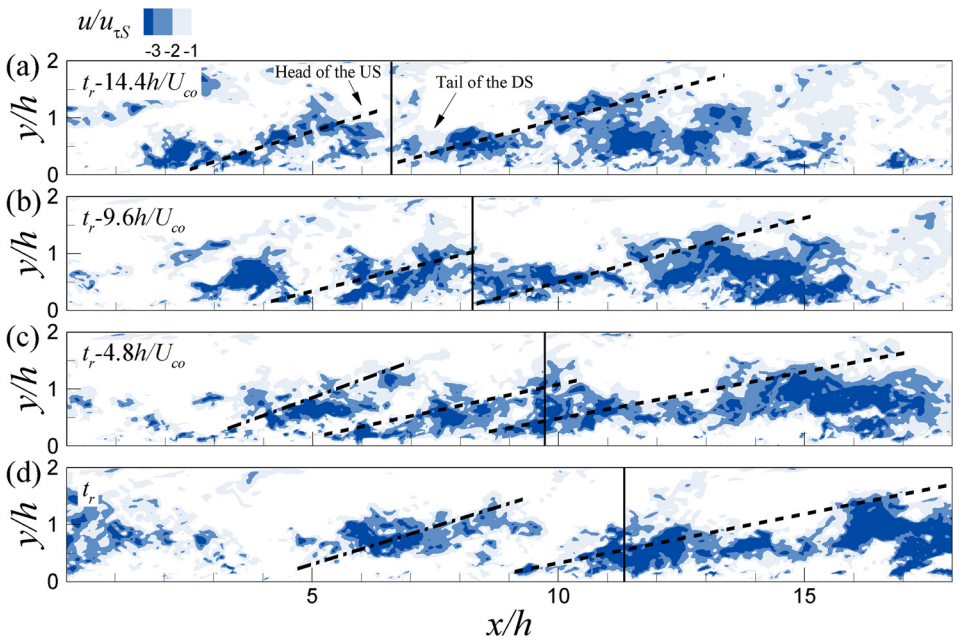

FIG. 10. Identical to those in Fig. 8, but for the CPR-flow. Dashed-dotted line indicates a new LSM in the upstream region of the VLSM.

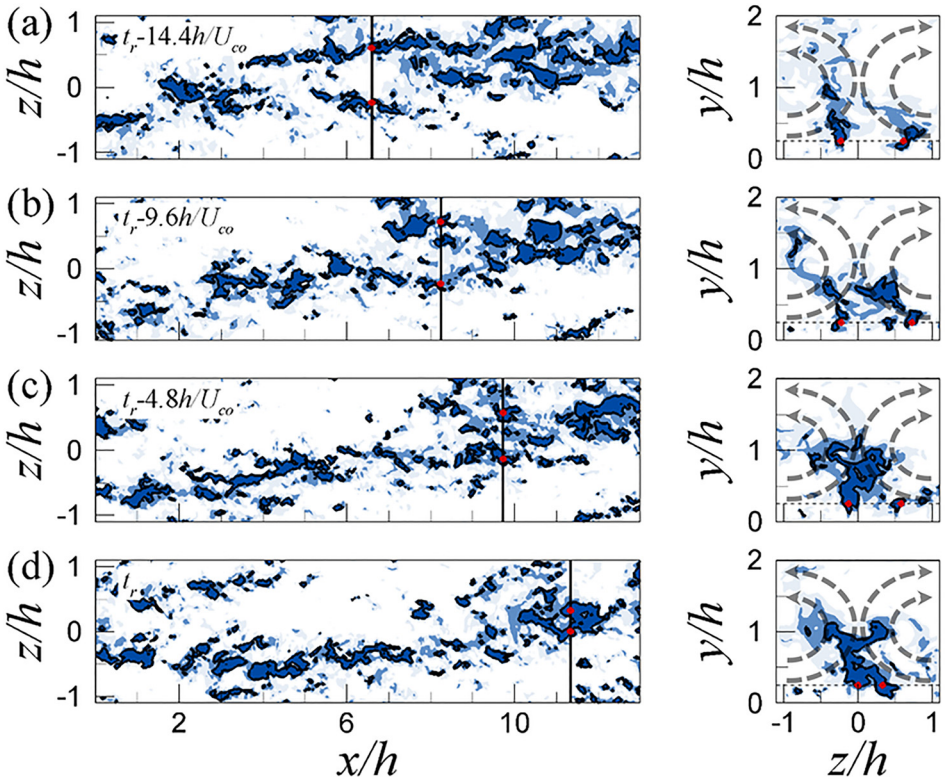

FIG. 11. Identical to those in Fig. 9, but for the CPR-flow. Horizontal dashed lines on the *yz*-plane ($y/h = 0.25$) indicate a location where the spanwise congregative motion of negative *u*-structures is dominant.

participating in the congregation motion (here, five streaks for the CP-flow and two steaks for the CPR-flow). Because the radius of the roll-cell motion for the CPR-flow is reduced due to the presence of surface roughness (compare the size of the semicircles on the *yz*-plane in Figs. 9 and 11), the number of the negative *u*-structures inducing the spanwise congregation becomes small in a narrow spanwise bound [see the outermost red circles at $t = t_r - 14.4h/U_{co}$ for the CP- and CPR-flows in Figs. 9(a) and 11(a)]. In addition, because the strength of the negative *u*-structures is generally high in the near-wall region due to the production of turbulence, the congregation motion of the negative *u*-structures with low strength in the outer layer for the CPR-flow can give rise to the generation of a weak large-scale ejection motion compared to that for the CP-flow, resulting in less retardation of the convection speed of the DS for the CPR-flow.

To demonstrate the presence of the high convection speed near the tail of the DS for the CPR-flow compared to that for the CP-flow, we estimate the local convection velocities (U_c) at the tail of the DS during the merging process for the CP- and CPR-flows. The local convection velocity is estimated using the convection distance (Δx_c), which is evaluated from the relative distance between local two peaks in a conditional autocorrelation coefficient of streamwise velocity fluctuations. The conditional autocorrelation coefficient is defined as follows (Lee *et al.*, 2014):

$$R_{uu}(x, y, z, t_r; x_r, y_r, z_r, t_r - \Delta t) = \frac{u(x_r, y_r, z_r, t_r - \Delta t)u(x, y, z, t_r)}{\sigma_u(x_r, y_r)\sigma_u(x, y)}, \tag{5}$$

where $\Delta t = 0.4h/U_{co}$ and x_r, y_r, and z_r refer to the reference point being the tail position of the DS. Because the correlation coefficient as a function of x ($y_r = y$ and $z_r = z$) shows local two peaks with a distance of Δx_c, the convection speed (U_c) is estimated simply using $\Delta x_c/\Delta t$.

Figure 12 shows the distributions of the local convection velocities of the tail of the DS during the merging process for the CP- and CPR-flows. As expected, the convection velocities of the tail of the DS

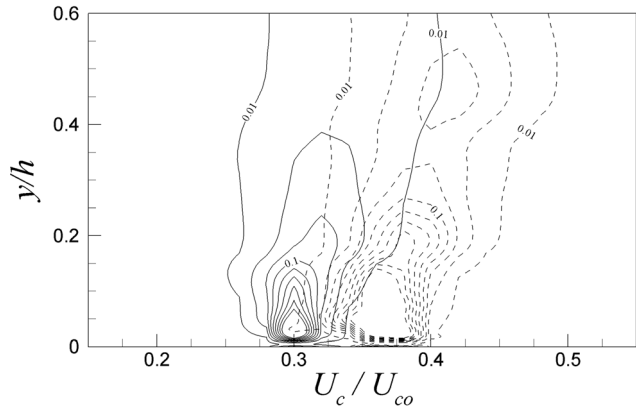

FIG. 12. Distributions of the local convection velocity (U_c) at the tail of the DS during the merging process for the CP- (solid lines) and CPR-flows (dashed lines). Contour levels are varied in the range of $0.01 \leq U_c/U_{co} \leq 0.25$ with an interval of 0.03.

for the CPR-flow (dashed lines) are higher than those for the CP-flow (solid lines) due to the weak large-scale ejection for the CPR-flow. Because the presence of higher convection velocities of the tail of the DS for the CPR-flow results in small difference in the convection velocity compared to the head of the US (residing in the outer layer), a frequency reduction of the merging between adjacent LSMs for the CPR-flow can be expected. Specifically, the merging frequencies of the LSMs (ρ_m) are estimated to 0.317 and 0.223 for the CP- and CPR-flows. Here, the merging frequency is defined as the average number of merging events between two LSMs relative to the total number of VLSMs observed in instantaneous fields for a sampling duration time of $2000h/U_{co}$ for each flow with a time interval of $0.4h/U_{co}$; the total number of VLSMs is evaluated using streaks longer than the streamwise length scale of $10h$ at given time. Although the value of ρ_m depends on the time interval and scale boundary, changing these values has no influence on the outcome (not shown here). The decreased merging frequency for the CPR-flow leads directly to the weakened VLSMs for the CPR-flow (Figs. 2 and 3).

To provide statistical evidence of the streamwise concatenation of LSMs for both flows, the merging process of VLSMs is conditionally sampled from a time series of DNS data. The time-evolving conditionally averaged velocity fields are defined as follows (Lee *et al.*, 2014):

$$\langle u|_m(x,y,z,t_r-\Delta t;x_r,y_r,z_r,t_r)\rangle = \langle u(x,y,z,t_r-\Delta t)|u^{DS}(x_r,y_r,z_r,t_r)\rangle, \quad (6)$$

where x_r, y_r, and z_r refers to the reference point being the tail position of the DS when a merging is complete at $t = t_r$. The reference wall-normal position for conditional averaging is set to the channel centerline ($y_r/h = 1.0$). The time series are obtained by conditionally averaging the velocity fields while varying Δt relative to the merging instance t_r. The time sequence of conditionally averaged flow fields, $\langle u|_m\rangle^+$, for a CP-flow is shown in Fig. 13. Here, the bold solid line indicates a relatively strong negative u-structure. Although the reference location for the conditional average is positioned on the centerline, the flow field at $t_r - 9.6h/U_{co}$ shows the tail of the DS at around $x/h = -0.5$. In addition, another velocity signature for a negative u-structure is captured upstream of the reference position. With time, these US and DS narrow their relative distance, creating a very-long negative u-structure. The time sequence of conditionally averaged flow fields on the

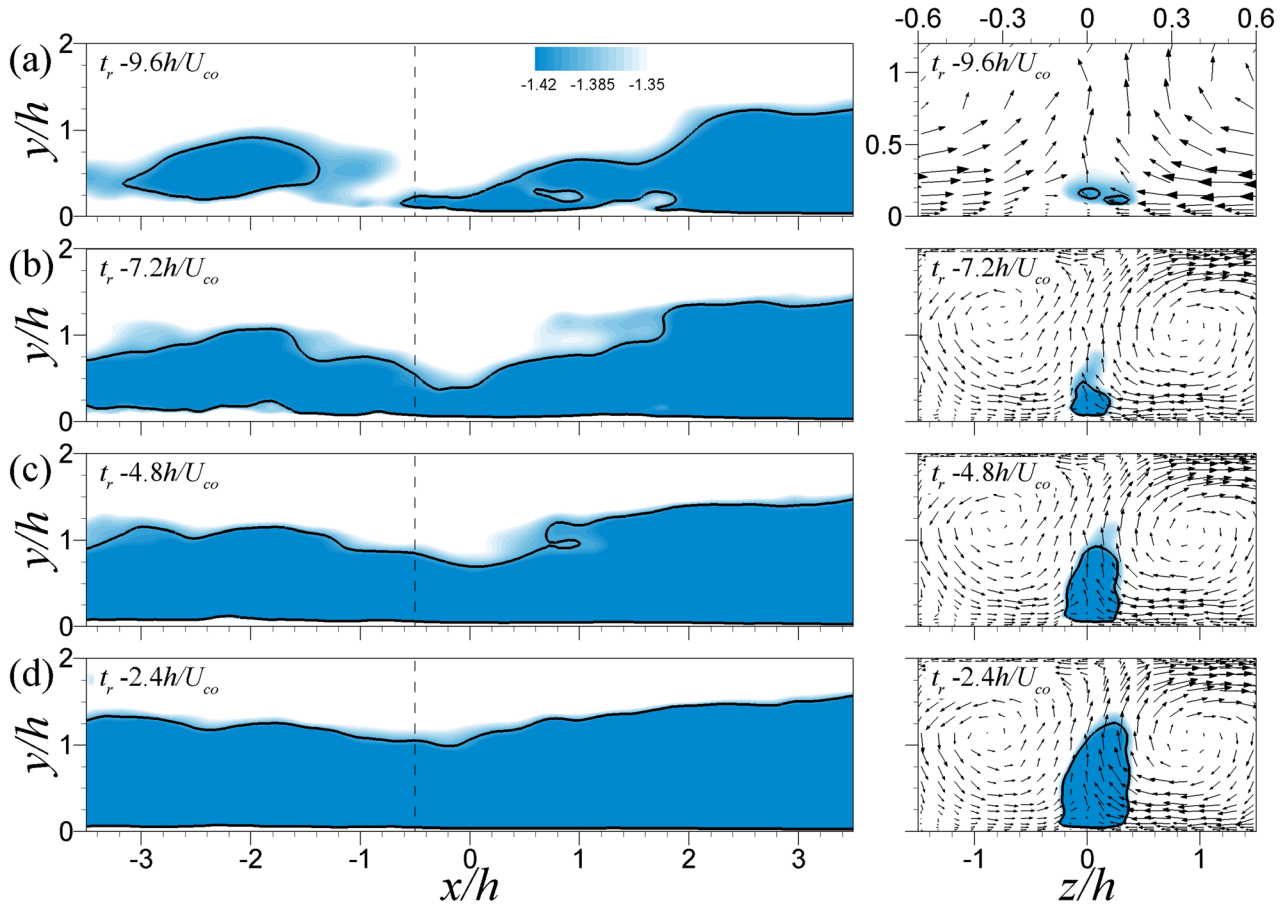

FIG. 13. Time sequence of conditionally averaged flow fields $\langle u|_m\rangle^+$ for the CP-flow. The wall-normal reference location for a merging event is $y_r/h = 1$. The flow fields on the yz-plane are extracted at a streamwise location ($x/h = -0.5$, black dashed lines) on the xy-plane. The bold solid line indicates $\langle u|_m\rangle^+ = -1.4$. Vectors on the yz-plane are constructed using conditionally estimated flow fields $\langle v|_m\rangle^+$ and $\langle w|_m\rangle^+$. Note that the yz-plane at $t_r - 9.6h/U_{co}$ is magnified to clarify the motion of the negative u.

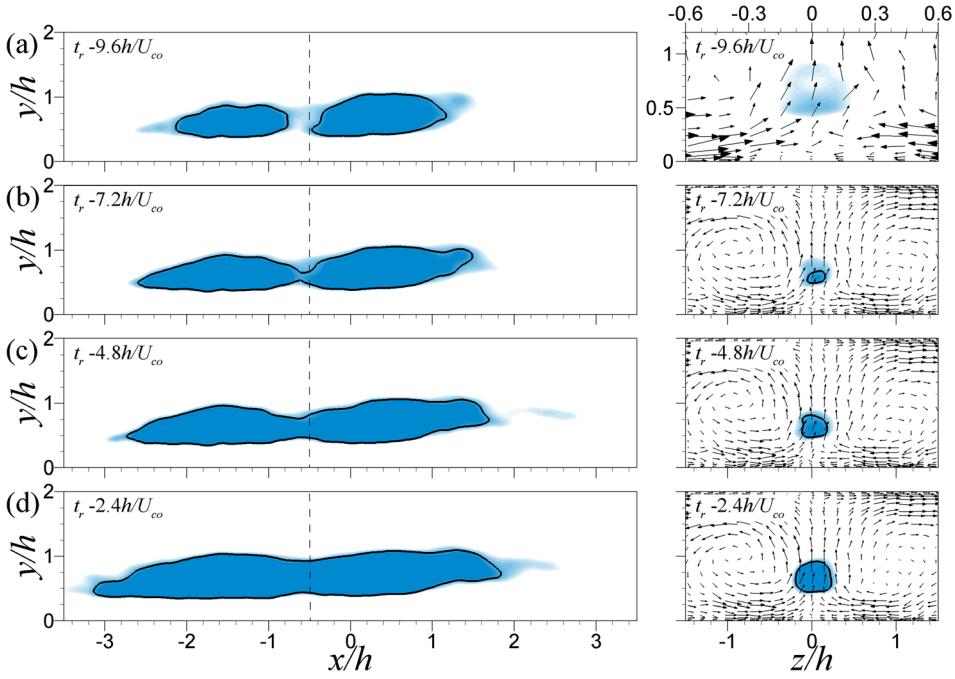

FIG. 14. Identical to those in Fig. 13, but for the CPR-flow.

yz-plane at a streamwise location at $x/h = -0.5$ in Fig. 13 shows that intensified near-wall negative u-structures near the tail of the DS are generated by the outer roll-cell motion. At $t_r - 9.6h/U_{co}$, there exists a pair of very-large-scale circulations of a roll-cell centered at $y/h = 1.0$. In addition, two distinct negative u-structures are found at $y/h = 0.1$–0.22. This roll-cell motion induces continuously spanwise congregation motion of the negative u-structures, eventually leading to a large-scale ejection of the streamwise velocity fluctuations which penetrates above the core region at $t_r - 2.4h/U_{co}$.

A time sequence of conditionally averaged flow fields for the CPR-flow in Fig. 14 shows a formation process of a VLSM similar to that for the CP-flow: two US and DS with a streamwise gap are streamwise-concatenated to form a VLSM. However, contrary to the LSMs for the CP-flow (Figs. 8 and 13), the two LSMs conditioned at $y_r/h = 1.0$ are detached from the wall with a relatively short streamwise length scale, consistent with the earlier finding in Fig. 10. Within the roughness sublayer, it is known that violent turbulent activities are frequently generated by the impingement of a flow into the surface roughness, creating large-scale ejecting motions into the outer layer with a large inclination angle to the wall (Volino *et al.*, 2009; Lee *et al.*, 2011). Although similar events are observed within the roughness sublayer for the CPR-flow (not shown here), the existence of the detached LSMs in Fig. 14 implies that near-wall u-structures for the CPR-flow do not contribute to the formation of the LSMs (and eventually the VLSM) near the centerline. On the yz-plane, a roll-cell motion centered in the channel centerline induces the congregation motion of negative u-structures. However, concentrated negative u-structures are found in the outer region. As a result, the large-scale ejection motion is obviously weakened, and the small difference in the convection velocities between the two LSMs caused by the weakened large-scale ejection results in the weakened VLSM via the less frequent merging of the LSMs to form a VLSM for the CPR-flow (Figs. 2 and 3). In Fig. 14, the strength of the roll-cell motion for the CPR-flow is also reduced compared to that for the CP-flow. In Sec. III B 3, we will show that the reduced strength of the roll-cells for the CPR-flow is attributed to the weakened VLSM.

3. Formation of roll-cell motions

In this section, first we extract the most energetic VLSM pattern (i.e., the POD mode), which mainly contributes to a flow, by considering the Karhunen–Loeve procedure from the eigenfunctions of the two-point correlation tensor in the Fourier domain (Moin and Moser, 1989; Duggleby *et al.*, 2007; Baltzer, 2012; Tutkun and George, 2017; Lee *et al.*, 2019),

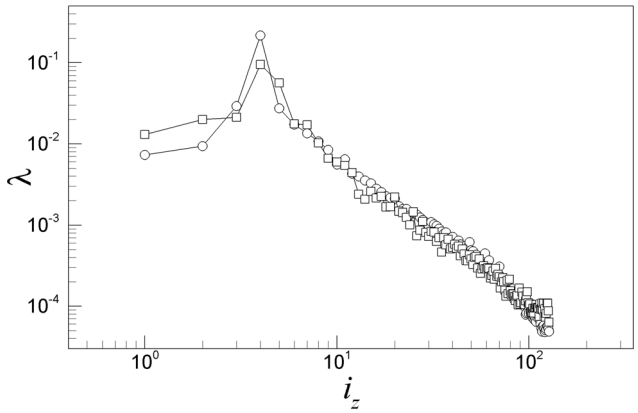

FIG. 15. Contribution to the total turbulent kinetic energy of the eigenmodes $\phi = (i_z, n)$. Here, only eigenvalues with $n = 1$ are presented: CP- (circle) and CPR-flows (square).

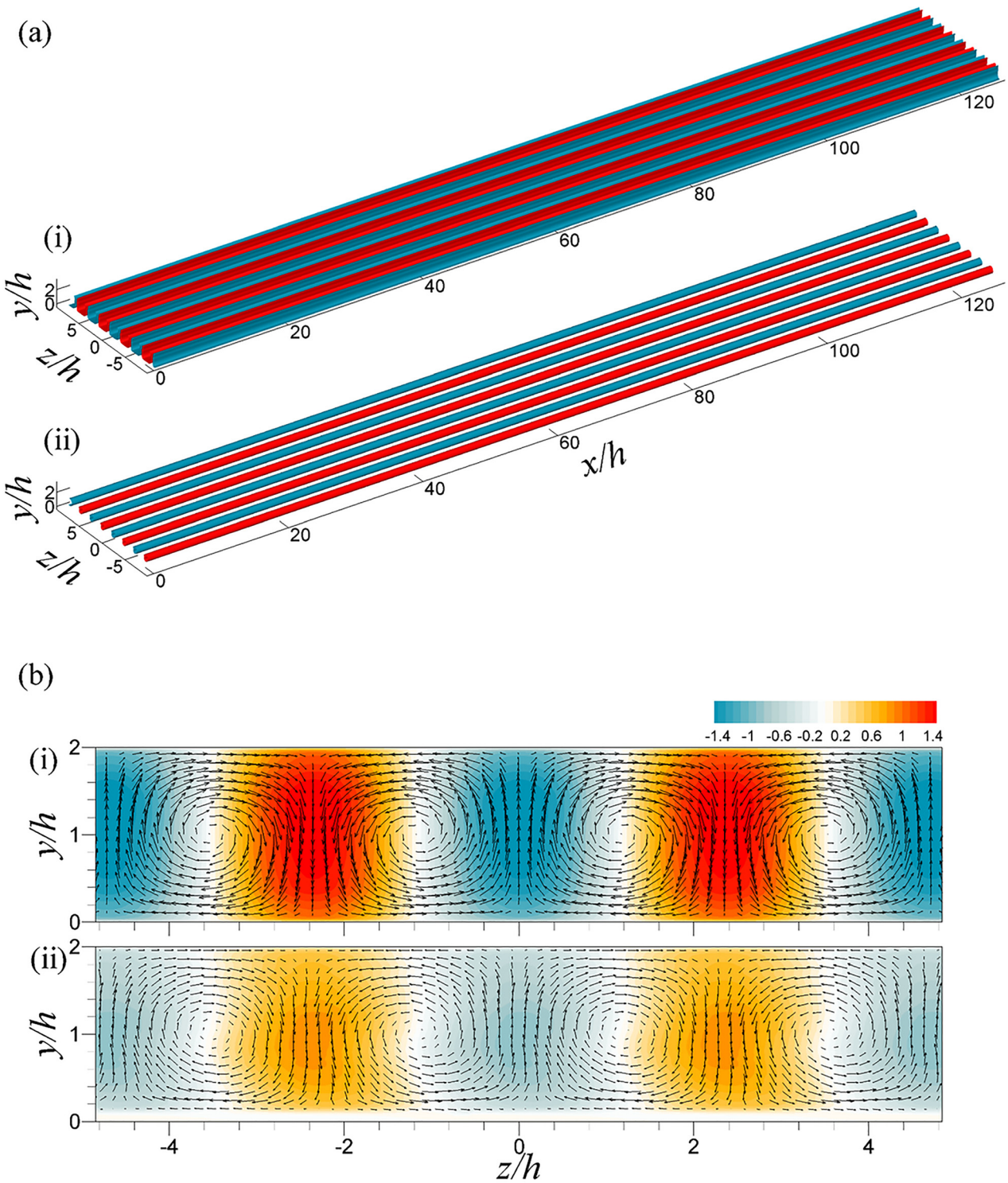

FIG. 16. Roll-cell-like behavior of the most energetic POD mode (a) in the trimetric view and (b) on the *yz*-plane at $x/h = 20\pi$: (i) CP- and (ii) CPR-flows (location I). Red and blue isosurfaces in (a) indicate the streaky patterns of positive and negative *u*-structures with $u/U_{\tau S} = \pm 0.5$. In (b), color contours of the reconstructed *u* with the in-plane velocity vectors of the *v* and *w* modes are presented. The centers of the roll-cell motions are observed at $(y/h, z/h) = (1.01, \pm 1.21)$ for the CP-flow and $(1.03, \pm 1.21)$ for the CPR-flow.

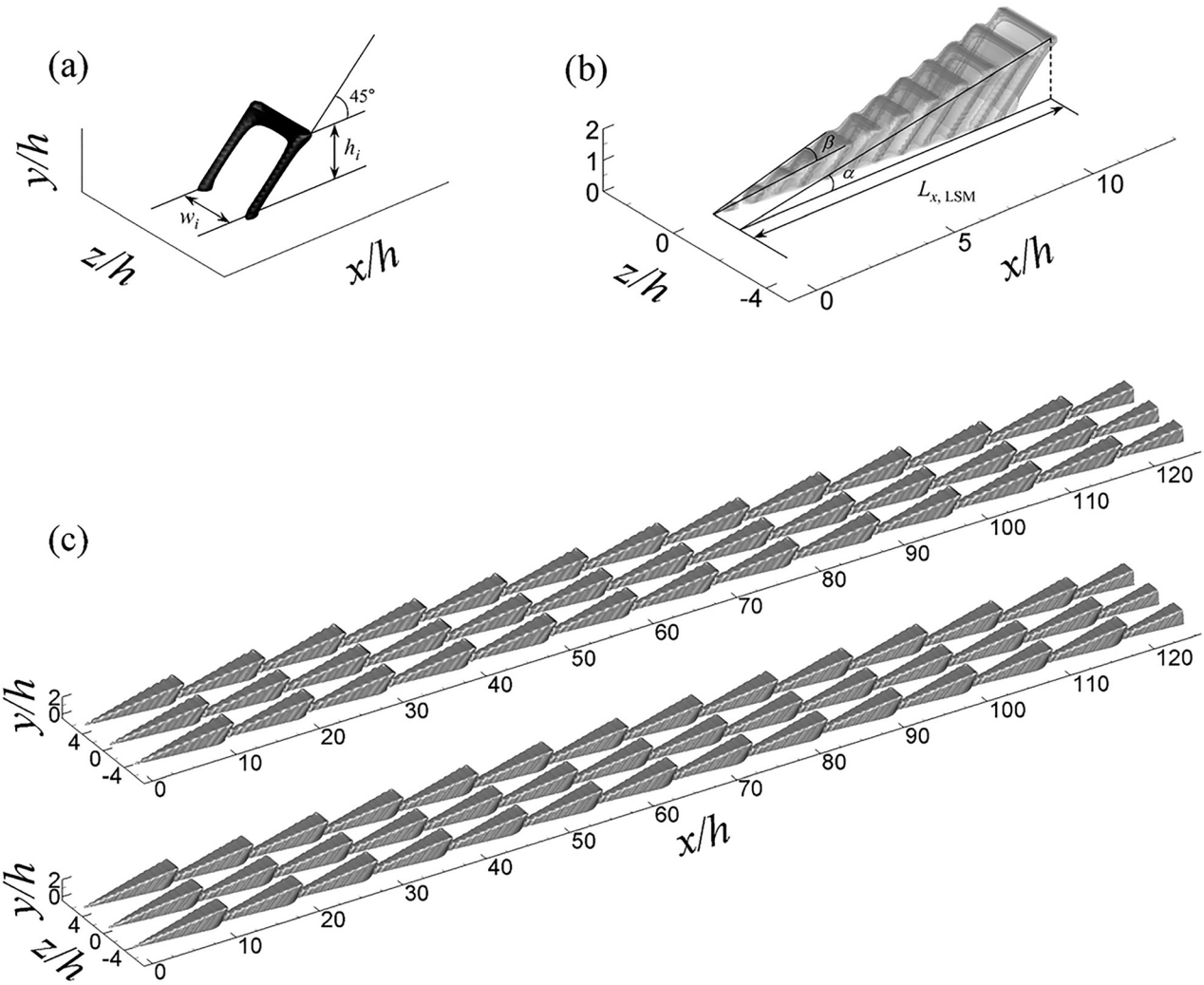

FIG. 17. (a) Goal-post-like model of a single hairpin vortex. An individual hairpin is inclined toward the flow direction at 45°. (b) Hairpin packet model (gray contour) for the CP-flow using 12 hairpin vortices. The isosurface contours in (a) and (b) are the negative streamwise velocity. The width (w_i) of each hairpin vortex varies linearly with the relationship $2.36hs^2i/n_h$, where i is the number of the ith hairpin vortex within a single hairpin packet and n_h is the total number of hairpin vortices embedded in a single hairpin packet. The height (h_i) is given with the relationship $2hs^2i/n_h$. The hairpin vortices in (b) are separated with a spacing of $0.806h$ (for the CP-flow) in the streamwise direction, creating a streamwise length scale of a hairpin packet, $L_{x,\,LSM}$. (c) Trimetric view of synthetically constructed VLSM patterns (u velocity with 20% of the minimum) associated with the most energetic POD modes for the CP- (top) and CPR-flows (bottom). The flow direction is from left to right.

$$\int_D S_{ij}(x,y,k_z;x_r,y_r)\hat{\phi}_j^{*(n)}(x,y,k_z)dy = \lambda^{(n)}(k_z)\hat{\phi}_i^{(n)}(x_r,y_r,k_z), \quad (7)$$

where $\hat{\phi}$ is the Fourier-transformed eigenfunction with the associated eigenvalue λ, $(^*)$ denotes the complex conjugate, and n is an index assigned to each POD mode by ordering with the decrease in the energy. This allows us to demonstrate that the very-large-scale circulation of the roll-cell mode is a direct consequence of pure kinematics within VLSMs according to the procedure in a turbulent pipe flow by Lee *et al.* (2019). The two-point spectral-density tensor S_{ij} is calculated using Fourier-transformed velocity fluctuations $\hat{u}_i(x,y,k_z)$ in the spanwise direction

$$S_{ij}(x,y,k_z;x_r,y_r) = \langle \hat{u}_i(x_r,y_r,k_z)\hat{u}_j^*(x,y,k_z)\rangle. \quad (8)$$

A POD analysis is conducted using all correlation components between the velocity fluctuations throughout the 3-D computational domain. Due to the homogeneity and periodicity in the spanwise direction for the CPR-flow, each POD mode is assigned a mode number set (i_z, n), where i_z is an index for which the corresponding mode wavelength is $\lambda_z = L_z/i_z$ ($L_z = 6\pi h$). In the latter, we will use both notations, (i_z, n) and (k_z, n), as convenient.

Because the eigenvalue indicates the mean amounts of turbulent kinetic energy contributed by each mode to reconstructed velocity fields, the most energetic modes with $n = 1$ are particularly important when organizing the flows. The estimated eigenvalues of the modes

TABLE III. Parameters for the construction of the hairpin packet model for CP- and CPR-flows.

Case	r_0/h	α	β	$L_{x,\,\mathrm{LSM}}/h$	n_h	d_h
CP-flow	0.053	11.68°	13.44°	9.67	12	0.806
CPR-flow	0.082	12.57°	14.75°	8.97	14	0.641

$n = 1$ for the CP- and CPR-flows are shown in Fig. 15. Note that the $n = 1$ eigenvalue spectra for each i_z in Fig. 15 include the sum of all Fourier modes with positive and negative values for each index. Although not shown here, it is found that the $n = 1$ modes for the CP- and CPR-flows account for more than 90% of the total kinetic energy for all i_z modes, consistent with previous studies in turbulent pipe flows by Baltzer *et al.* (2013) and Lee *et al.* (2019). The most energetic POD mode for both flows is observed at a spanwise wavenumber of $i_z = 4$, indicating that the most energetic coherent structure with an average spanwise distance of $\lambda_z = 6\pi h/i_z = 4.71h$ is important when organizing the entire flow; moreover, this spanwise distance is very similar to that between the negative (or positive) VLSMs for the CP- and CPR-flows in Fig. 2. The similarity between the most energetic POD mode and the time-averaged fields suggests that the entire flow features for both the CP- and CPR-flows are mostly determined by VLSM patterns. Although the most energetic modes for the CP- and CPR-flows are found at an identical wavenumber, the peak values of the eigenvalue for the flows show some discrepancy: $\lambda = 0.216$ for the CP-flow and $\lambda = 0.094$ for the CPR-flow. The smaller contribution to the total kinetic energy for the CPR-flow indicates that the most energetic motion for the CPR-flow makes less of a contribution to the total flow. The VLSMs with long wavelength ($i_z < 4$) for the CPR-flow make a large energy contribution compared to that for the CP-flow. For motions with small scales ($i_z > 4$), the energy spectra for both the CP- and CPR-flows are well collapsed with decaying behavior, showing cascades of kinetic energy from large- to small-scale motions.

Figure 16 displays the isosurfaces of the reconstructed u mode with the vector patterns of the reconstructed v and w modes for the most energetic POD mode for the CP- and CPR-flows, i.e., $(i_z, n) = (4, 1)$. For both flows, very-large-scale streaky patterns associated with roll-cells are periodically arranged along with the spanwise domain. The spanwise spacing between the very-large-scale streaky (or roll-cell) patterns is approximately $4.71h$, consistent with our observation in Fig. 2. It is noted that for a turbulent channel flow, the spanwise spacing between roll-cells is smaller than that for the CP-flow due to relatively small size of the structures (Abe *et al.*, 2018). A direct comparison of the VLSMs and roll-cells between the CP- and CPR-flows shows the weakened state of the structures for the CPR-flow, similar to our observations in Figs. 2, 3, 13, and 14. In addition, although roll-cell motions influence near-wall structures for both flows, the introduction of surface roughness weakens the influence of the roll-cells on the near-wall region, consistent with our observations in Figs. 5, 6, 7, 9, and 11. In Fig. 16, the most dominant patterns are those of the roll-cells, indicating a close association with VLSMs. However, although much effort was devoted to studying roll-cell-like motions in previous studies using various approaches (Toh and Itano, 2005; del Álamo and Jiménez, 2006; Hutchins and Marusic, 2007; Chung and McKeon, 2010; Baltzer *et al.*, 2013), the origin of the roll-cells remains unclear.

To investigate how the spatial organization pattern of roll-cells is created in the flow field based on the model of VLSMs in Fig. 16 (as a possible candidate), we consider the hairpin model proposed by Perry and Chong (1982) and Perry and Marusic (1995). In their model, a hairpin has the shape of a goal-post inclined at 45° to the wall in the downstream direction, creating a velocity by induction based on the Biot–Savart law. Here, we approximate the VLSM pattern for the CP- and CPR-flows as the streamwise concatenations of hairpin packet-like LSMs (Figs. 8 and 10), and the LSMs consist of coherently aligned goal-post hairpins. The modifications of the VLSM pattern by surface roughness are reflected in the model simply by changing the vortex core radius of the hairpins (r_0) and the configuration of the hairpin vortices, i.e., the inclination angle (α) of the hairpin packet-like LSMs to the wall and the streamwise spacing (d_h) between the hairpins to form a LSM (see the detailed description in the Appendix).

Figure 17(a) shows the typical structure of a goal-post-like hairpin model represented by an isosurface with a minimum velocity of 20%. The legs of the hairpin are attached to the wall, and the inclination angle of the structure is held constant at 45° for both flows. To consist of a hairpin vortex packet in Fig. 17(b), the height (h_i) of the hairpins for the CP-flow varies linearly with the relationship $2hs^2i/n_h$, creating a packet that grows continuously from the bottom wall to the top wall with a mean inclination angle of approximately $\alpha = 11.68°$ (Pirozzoli *et al.*, 2011; Kim *et al.*, 2020). Here, i is the number of the i^{th} hairpin vortex within a single hairpin packet and n_h is the total number of hairpin vortices embedded in a packet. For the CPR-flow, the height of h_i also varies linearly ($2hs^2i/n_h$) with a mean inclination angle of a packet with $\alpha = 12.57°$ (see the Appendix). Based on the inclination angles for the CP- and CPR-flows, the streamwise extent of a LSM for each flow, $L_{x,\,\mathrm{LSM}}$, is determined to be $9.67h$ for the CP-flow

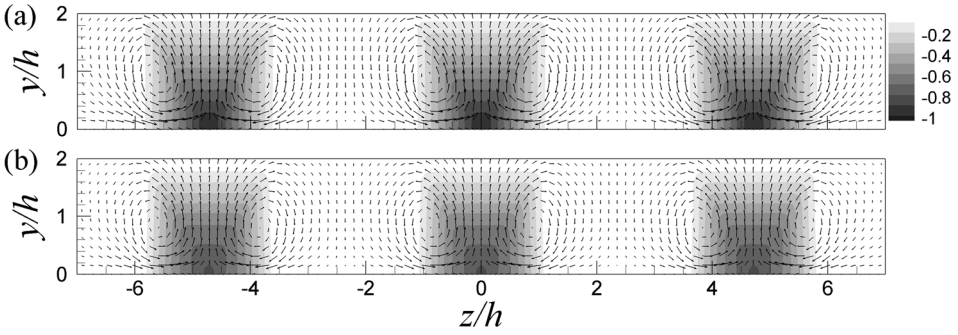

FIG. 18. Spatial organization patterns of hairpin packet models for the (a) CP- and (b) CPR-flows shown in Fig. 17(c). The flow fields are streamwise-averaged over a single LSM for each case, i.e., $L_{x,\,\mathrm{LSM}}$. To clarify the relative magnitudes, both plots are normalized by the magnitude of minimum streamwise velocity for the CP-flow.

and $8.97h$ for the CPR-flow using the relationship $L_{x,\,\mathrm{LSM}} = 2h/\tan(\alpha)$. Given that the streamwise distances (d_h) between hairpins within a packet are estimated to be $0.806h$ for the CP-flow and $0.641h$ for the CPR-flow based on linear estimates of the conditional velocity field with a spanwise swirling event (see the Appendix), hairpin vortex packets with a streamwise length of $L_{x,\,\mathrm{LSM}}$ for the CP- and CPR-flows consist of approximately $n_h = 12$ and 14 hairpin vortices that are streamwise-aligned. The spanwise width (w_i) of hairpins within a packet varies linearly with the relationship $2.36hs^2i/n_h$ for both flows, as the streaky patterns of the VLSMs shown in Fig. 16 are characterized by a spanwise scale of $\sim 2.36h$. This leads to a spanwise growth angle of β for both flows, as β is defined by $\beta = \tan^{-1}(w_i \sin(\alpha)/h_i)$

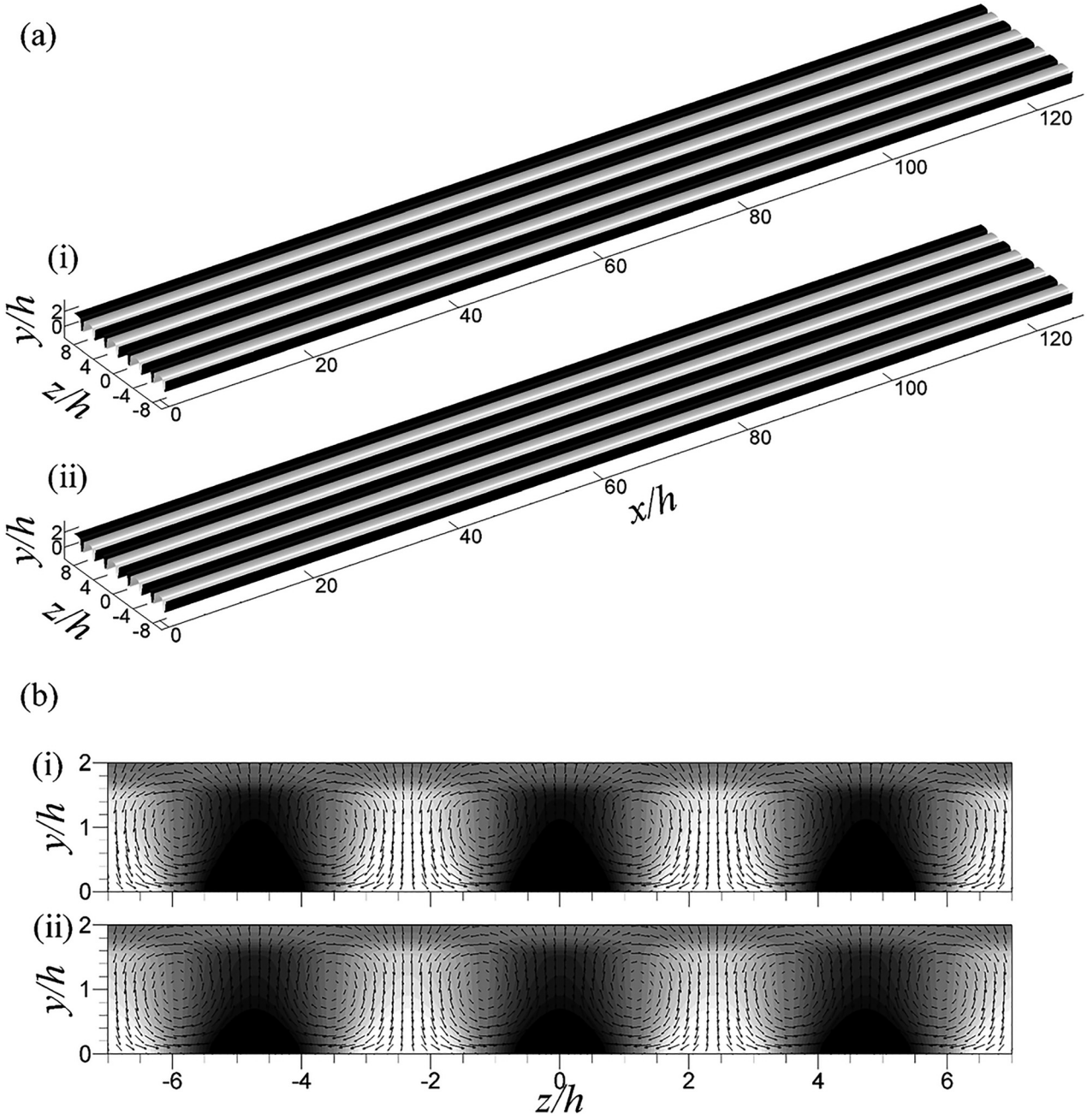

FIG. 19. The induced roll-cell-like behavior by the POD mode of the artificially constructed VLSM patterns (a) in the trimetric view and (b) on the *yz*-plane at $x/h = 20\pi$: (i) CP- and (ii) CPR-flows (I). White and black isosurfaces indicate the streaky patterns of positive and negative *u*-structures (at 20% of maximum and minimum). In (b), color contours of the reconstructed *u* with the in-plane velocity vectors of the *v* and *w* modes are presented.

based on the geometrical relationship within a packet. The parameters that constitute the hairpin packet models for the CP- and CPR-flows are summarized in Table III. The induced velocity within and around a packet is simply the linear summation of the velocities induced by the individual hairpin vortices. In Fig. 17(c), the packet-like LSMs are aligned in the streamwise direction with no spanwise offset to construct the most energetic VLSMs patterns observed in Fig. 16 for the CP- and CPR-flows. Because the LSMs are aligned throughout the streamwise domain, 13 and 14 hairpin packets are employed to construct a single VLSM for the CP- and CPR-flows, respectively. The spanwise offset spacing between the very-large-scale streaky patterns is $\lambda_z = 4.71h$ for both flows according to the results from the time-averaged flow field and the POD modes in Figs. 2 and 16.

The velocity patterns induced by the artificially constructed VLSMs for the CP- and CPR-flows are shown in Fig. 18. It is evident that the streamwise-aligned LSMs mimicking the most energetic VLSMs for the CP- and CPR-flows induce the spatial organization patterns of roll-cells, similar to those found in the time-averaged flow fields and POD mode (Figs. 2 and 16); that is, low-speed VLSM flanked by counter-rotating roll-cells. However, compared to our observation from the POD mode in Fig. 16, the centers of the in-plane circulations around the reference point are $(y/h, z/h) = (0.89, \pm 0.92)$ for the CP-flow and $(0.91, \pm 0.87)$ for the CPR-flow, and the streamwise velocity field in the near-wall region is unnecessarily intensified due to the large role of the attached hairpins in our model and the absence of surface roughness for the CPR-flow. The overall magnitude of the roll-cell patterns is weakened for the CPR-flow; for example, the magnitude of the roll-cells at the location $(y/h, z/h) = (0.7, 0.5)$, where the strongest upward motion of the roll-cells exists for the CPR-flow, is 20% lower than that for the CP-flow. These weakened roll-cell patterns for the CPR-flow are mostly induced by the increased vortex core radius (r_0) compared to that for the CP-flow.

Figure 19 shows POD modes constructed using the artificially constructed VLSM patterns [Fig. 17(c)] of the most energetic mode for the CP- and CPR-flows. As expected, this approach results in the most energetic $n = 1$ POD mode with a dominant wavenumber of $i_z = 4$. The very-large-scale counter-rotating roll-cell-like vortex patterns are periodically organized in the spanwise direction, similar to our previous observation. However, the isosurfaces of the VLSMs in the figure are not closed in the near-wall region for both flows (see the trimetric view), indicating that the model for the VLSMs to construct the roll-cells is not complete. This is attributable to the absence of the consideration not only the interaction between the inner and outer layers (Mathis *et al.*, 2009) but also of the hierarchy of the scales across most of the wall layer in this model (Perry and Marusic, 1995; Adrian *et al.*, 2000). The generation of the roll-cells in Fig. 19 (similar to the actual ones in Figs. 2 and 16) demonstrates that roll-cells for the CP-flow (and for the CPR-flow) can be created by VLSMs that are collectively formed by the streamwise concatenation of the LSMs. The weakened roll-cell pattern for the CPR-flow in Figs. 18 and 19 is a direct consequence of the weakened VLSM pattern. In other words, the generation of the weakened VLSMs by surface roughness for the CPR-flow leads to weakened roll-cells or very-large-scale circulations.

IV. SUMMARY AND CONCLUSIONS

In the present study, we analyzed a DNS dataset of fully developed turbulent Couette–Poiseuille flows over the smooth and rough walls to examine the modification of the overall process for the formation of VLSMs and roll-cell motions near the centerline by surface roughness. For the CP-flow, collective behavior of negative u-structures in the near-wall region was found due to the circulation of roll-cells centered in the channel core. The introduction of surface roughness into the flow led to the suppression of the near-wall spanwise congregation motions, and strong congregation motion was observed to occur in the outer layer ($y/h = 0.25$) for the CPR-flow. The formation process for the VLSMs for the CP-flow was very similar to that observed in previous studies for turbulent channel/pipe and boundary layer flows: the VLSM is created by the streamwise concatenation of LSMs due to the difference of the convection speed between the upstream and downstream LSMs. The slow speed of the tail of the downstream LSM was closely associated with the generation of a strong large-scale ejection, which was formed by the spanwise congregative motions of the near-wall streaks. Although a similar process for the formation of the VLSMs was observed for the CPR-flow, the presence of a weak large-scale ejection motion reduced the merging frequency between adjacent LSMs, thus ultimately weakening the VLSMs for the CPR-flow. The weak large-scale ejection for the CPR-flow was explained by the reduced radius of the roll-cell motion caused by the surface roughness. Because the reduced radius of the roll-cell motion led to collective spanwise motion of a small number of negative u-structures in the outer layer, the strength of the large-scale ejection for the CPR-flow became lower than that for the CP-flow, resulting in a smaller difference in the convection speed between the upstream and downstream LSMs. Based on the hairpin model by Perry and Chong (1982) and Perry and Marusic (1995), we showed that roll-cell-like motions for the CP- and CPR-flows are created by VLSMs that are collectively constructed by means of LSM concatenation. Thus, the weakened roll-cell-like patterns for the CPR-flow were a direct consequence of the weakened VLSM patterns.

ACKNOWLEDGMENTS

This research was supported by the National Research Foundation of Korea (NRF) funded by the Ministry of Education (Grant No. NRF-2019R1A2C1083858).

APPENDIX: CONSTRUCTION OF SYNTHETIC VLSM PATTERNS

In Sec. III B 3, a streamwise spacing between hairpin vortices to form a LSM for each flow is determined by means of a linear stochastic estimation for the conditional averaging of the velocity fields with the event of the swirling strength (λ_{ci}) on the xy-plane (Christensen and Adrian, 2001),

$$\langle u_i(x,y)|\lambda_{ci}(x_r,y_r)\rangle \approx L_i\lambda_{ci}(x_r,y_r), \tag{A1}$$

where

$$L_i = \frac{\langle \lambda_{ci}(x_r,y_r)u_i(x,y)\rangle}{\langle \lambda_{ci}(x_r,y_r)^2\rangle}. \tag{A2}$$

Figure 20 shows the conditionally averaged velocity vector fields on the xy plane (i.e., spanwise-oriented vortex pattern) for the CP- and CPR-flows when $x = x_r = 20\pi h$. The magnitude of the vectors is set

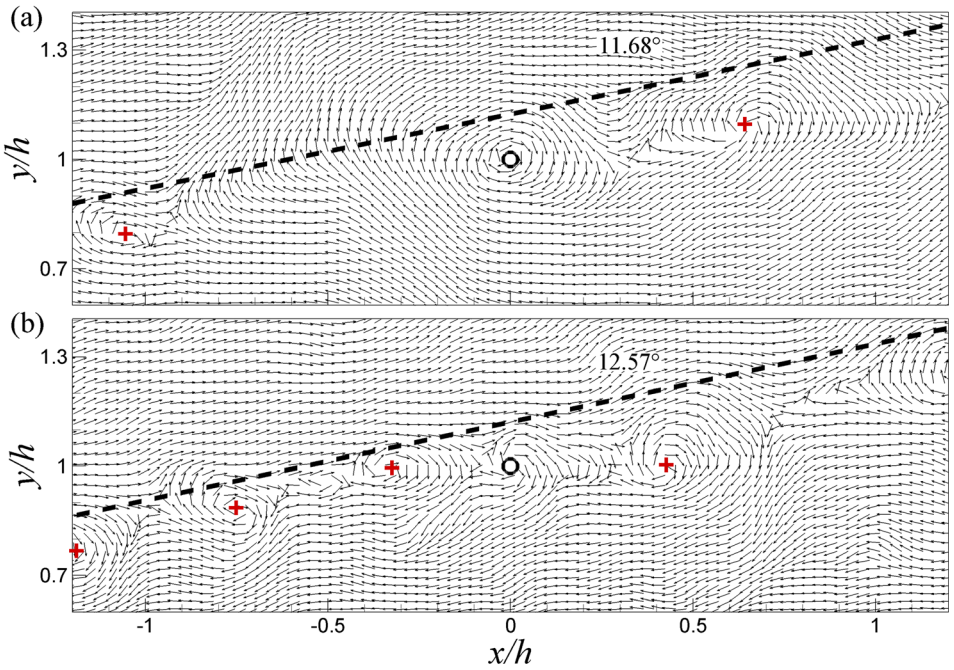

FIG. 20. Linear estimates of conditional velocity fields conditioned by a spanwise swirling strength event in the channel centerline ($y_c/h = 1$) on the *xy*-plane: (a) CP- and (b) CPR-flows. The open circle symbols indicate the wall-normal reference locations and red cross symbols indicate vortex cores residing in the upstream and downstream locations with respect to $x/h = 0$.

to unit to represent relatively weak motion away from the event location clearly. For the CP-flow in Fig. 20(a), a shear layer is inclined at an angle of ∼12° away from the bottom wall, and the velocity beneath the shear layer is negative and positive above the shear layer. The mean streamwise distance between the vortices along the positive–negative interface is estimated to be 0.806*h* for the CP-flow. The appearance of the velocity vector fields for the CPR-flow is similar to that for the CP-flow. However, the inclination angle of the interface increases slightly to approximately 13°. In addition, the average streamwise distance between the vortices for the CPR-flow decreases to 0.641*h*. The decreased streamwise distance between vortices is consistent with previous observations in the outer region of TBL and Poiseuille flows with rod roughness (Nagano *et al.*, 2004; Lee *et al.*, 2011).

In Fig. 21, the linearly estimated vortex pattern with the event of positively signed swirling strength is illustrated on the *xy*-plane for the CP- and CPR-flows. Here, the signed swirling strength is defined as $\Lambda_{ci} = \lambda_{ci}\omega_z|\omega_z|$, where ω_z denotes the spanwise vorticity

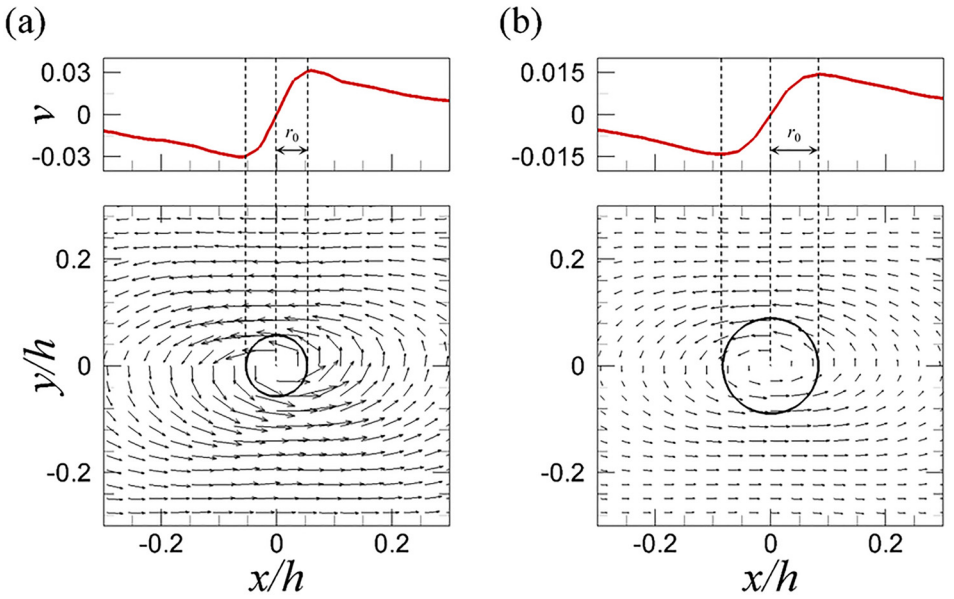

FIG. 21. Linear estimates of the conditional velocity fields conditioned by a positively signed swirling strength event in the channel centerline ($y_c/h = 1$) on the *xy*-plane: (a) CP- and (b) CPR-flows. The wall-normal velocity (v) along the line of $y/h = 0.0$ is depicted in the 1-D plot (red lines), and an estimated vortex pattern with its core radius (r_0) is shown in the contours.

(Natrajan *et al.*, 2007). To extract the average radius of the hairpin vortex for each flow, a Lamb-Oseen vortex model is fitted to the estimated velocity field (Stanislas *et al.*, 2008). The wall-normal velocity (v) along the line of $y/h = 0$ in Fig. 21 is assumed to be approximated by a tangential velocity component (v_θ) in polar coordinates

$$v \approx v_\theta = \frac{\Gamma}{2\pi r}\left[1 - e^{-\left(\frac{r}{r_0}\right)^2}\right], \tag{A3}$$

where Γ is the circulation by a given vortex. In the Lamb-Oseen vortex model, the vortex core radius (r_0) is estimated using a local extreme point (r_{max}) where the maximum or minimum velocity is obtained. By setting the derivative of (A3) with respect to r equal to zero, an equation to find r_{max} can be written as

$$1 - e^{-\left(\frac{r_{\max}}{r_0}\right)^2} = 2\left(\frac{r_{\max}}{r_0}\right)^2\left[e^{-\left(\frac{r_{\max}}{r_0}\right)^2}\right]. \tag{A4}$$

Solving the equation by iteration gives a value of $r_{max} \approx 1.12r_0$, corresponding to $r_{max} \approx 0.059h$ and $0.092h$ for the CP- and CPR-flows, respectively. The estimated value of r_0 for each flow is listed in Table III. The increased size of the vortex pattern for the CPR-flow compared to the CP-flow is consistent with an earlier finding in a TBL flow with rod roughness by Volino *et al.* (2009).

DATA AVAILABILITY

The data that support the findings of this study are available from the corresponding author upon reasonable request.

REFERENCES

Abe, H., Antonia, R. A., and Toh, S., "Large-scale structures in a turbulent channel flow with a minimal streamwise flow unit," J. Fluid Mech. **850**, 733–768 (2018).

Adrian, R. J., Meinhart, C. D., and Tomkins, C. D., "Vortex organization in the outer region of the turbulent boundary layer," J. Fluid Mech. **422**, 1–54 (2000).

Ahn, J., Lee, J. H., Jang, S. J., and Sung, H. J., "Direct numerical simulations of fully developed turbulent pipe flows for $Re_\tau = 180$, 544 and 934," Intl. J. Heat Fluid Flow **44**, 222–228 (2013).

del Álamo, J. C., and Jiménez, J., "Linear energy amplification in turbulent channels," J. Fluid Mech. **559**, 205–213 (2006).

Ashrafian, A., Andersson, H. I., and Manhart, M., "DNS of turbulent flow in a rod-roughened channel," Intl. J. Heat Fluid Flow **25**, 373–383 (2004).

Avsarkisov, V., Hoyas, S., Oberlack, M., and García-Galache, J. P., "Turbulent plane Couette flow at moderately high Reynolds number," J. Fluid Mech. **751**, R1 (2014).

Bakken, O. M., Krogstad, P. Å., Ashrafian, A., and Andersson, H. I., "Reynolds number effects in the outer layer of the turbulent flow in a channel with rough walls," Phys. Fluids **17**, 065101 (2005).

Baltzer, J. R., "Structure and proper orthogonal decomposition in simulations of wall-bounded turbulent shear flows with canonical geometries," Ph.D. thesis (Arizona State University, 2012).

Baltzer, J. R., Adrian, R. J., and Wu, X., "Structural organization of large and very large scales in turbulent pipe flow simulation," J. Fluid Mech. **720**, 236–279 (2013).

Bech, K., Tillmark, N., Alfredsson, P., and Andersson, H., "An investigation of turbulent plane Couette flow at low Reynolds numbers," J. Fluid Mech. **286**, 291–325 (1995).

Burattini, P., Leonardi, S., Orlandi, P., and Antonia, R. A., "Comparison between experiments and direct numerical simulations in a channel flow with roughness on one wall," J. Fluid Mech. **600**, 403–426 (2008).

Christensen, K. T., and Adrian, R. J., "Statistical evidence of hairpin vortex packets in wall turbulence," J. Fluid Mech. **431**, 433–443 (2001).

Chung, D., and McKeon, B. J., "Large-eddy simulation of large-scale structures in long channel flow," J. Fluid Mech. **661**, 341–364 (2010).

Dennis, D. J. C., and Nickels, T. B., "Experimental measurement of large-scale three-dimensional structures in a turbulent boundary layer. Part 1. Vortex packets," J. Fluid Mech. **673**, 180–217 (2011).

Djenidi, L., Elavarasan, R., and Antonia, R. A., "The turbulent boundary layer over transverse square cavities," J. Fluid Mech. **395**, 271–294 (1999).

Duggleby, A., Ball, K. S., Paul, M. R., and Fischer, P. F., "Dynamical eigenfunction decomposition of turbulent pipe flow," J. Turbul. **8**(43), 1–24 (2007).

Flack, K. A., Schultz, M. P., and Connelly, J. S., "Examination of a critical roughness height for outer layer similarity," Phys. Fluids **19**, 095104 (2007).

Gandía-Barberá, S., Hoyas, S., Oberlack, M., and Kraheberger, S., "Letter: The link between the Reynolds shear stress and the large structures of turbulent Couette–Poiseuille flow," Phys. Fluids **30**, 041702 (2018).

Hamilton, J. M., Kim, J., and Waleffe, F., "Regeneration mechanisms of near-wall turbulence structures," J. Fluid Mech. **287**, 317–348 (1995).

Hutchins, N., and Marusic, I., "Large-scale influences in near-wall turbulence," Philos. Trans. R. Soc. London A **365**, 647–664 (2007).

Hwang, J., Lee, J., Sung, H. J., and Zaki, T. A., "Inner–outer interactions of large-scale structures in turbulent channel flow," J. Fluid Mech. **790**, 128–157 (2016).

Hwang, Y., and Cossu, C., "Self-sustained processed at large scales in turbulent channel flow," Phys. Rev. Lett. **105**(4), 044505 (2010).

Jiménez, J., "Turbulent flows over rough walls," Annu. Rev. Fluid Mech. **36**, 173–196 (2004).

Kim, J. H., and Lee, J. H., "Direct numerical simulation of a turbulent Couette–Poiseuille flow: Turbulent statistics," Intl. J. Heat Fluid Flow **72**, 288–303 (2018).

Kim, J. H., Hwang, J. H., Lee, Y. M., and Lee, J. H., "Direct numerical simulation of a turbulent Couette–Poiseuille flow, Part 2: Large- and very-large-scale motions," Intl. J. Heat Fluid Flow **86**, 108687 (2020).

Kim, K. C., and Adrian, R. J., "Very large-scale motion in the outer layer," Phys. Fluids **11**, 417–422 (1999).

Kitoh, O., Nakabyashi, K., and Nishimura, F., "Experimental study on mean velocity and turbulence characteristics of plane Couette flow: Low-Reynolds-number effects and large longitudinal vortical structure," J. Fluid Mech. **539**, 199–227 (2005).

Komminaho, J., Lundbladh, A., and Johansson, A., "Very large structures in plane turbulent Couette flow," J. Fluid Mech. **320**, 259–259 (1996).

Krogstad, P. Å., and Antonia, R. A., "Surface roughness effects in turbulent boundary layers," Exp. Fluids **27**, 450–460 (1999).

Lee, J., Lee, J. H., Choi, J.-I., and Sung, H. J., "Spatial organization of large- and very-large-scale motions in a turbulent channel flow," J. Fluid Mech. **749**, 818–840 (2014).

Lee, J. H., and Sung, H. J., "Very-large-scale motions in a turbulent boundary layer," J. Fluid Mech. **673**, 80–120 (2011).

Lee, J. H., Sung, H. J., and Adrian, R. J., "Space–time formation of very-large-scale motions in turbulent pipe flow," J. Fluid Mech. **881**, 1010–1047 (2019).

Lee, J. H., Sung, H. J., and Krogstad, P. Å., "Direct numerical simulation of the turbulent boundary layer over a cube-roughened wall," J. Fluid Mech. **669**, 397–431 (2011).

Lee, M., and Moser, R. D., "Extreme-scale motions in turbulent plane Couette flows," J. Fluid Mech. **842**, 128–145 (2018).

Lee, S.-H., and Sung, H. J., "Direct numerical simulation of the turbulent boundary layer over a rod-roughened wall," J. Fluid Mech. **584**, 125–146 (2007).

Lee, Y. M., Kim, J. H., and Lee, J. H., "Direct numerical simulation of a turbulent Couette–Poiseuille flow with a rod-roughened wall," Phys. Fluids **30**, 105101 (2018).

Leonardi, S., Orlandi, P., Smalley, R. J., Djenidi, L., and Antonia, R. A., "Direct numerical simulations of turbulent channel flow with transverse square bars on the wall," J. Fluid Mech. **491**, 229–238 (2003).

Mathis, R., Monty, J. P., Hutchins, N., and Marusic, I., "Comparison of large-scale amplitude modulation in turbulent boundary layers, pipes, and channel flows," Phys. Fluids **21**, 111703 (2009).

McKeon, B. J., and Sharma, A. S., "A critical-layer framework for turbulent pipe flow," J. Fluid Mech. **658**, 336–382 (2010).

Moin, P., and Moser, R. D., "Characteristic-eddy decomposition of turbulence in a channel," J. Fluid Mech. **200**, 471–509 (1989).

Nadeem, M., Lee, J. H., Lee, J., and Sung, H. J., "Turbulent boundary layers over sparsely-spaced rod-roughened walls," Intl. J. Heat Fluid Flow **56**, 16–27 (2015).
Nagano, Y., Hattori, H., and Houra, T., "DNS of velocity and thermal fields in turbulent channel flow with transverse-rib roughness," Intl. J. Heat Fluid Flow **25**, 393–403 (2004).
Natrajan, V. K., Wu, Y., and Christensen, K. T., "Spatial signatures of retrograde spanwise vortices in wall turbulence," J. Fluid Mech. **574**, 155–167 (2007).
Orlandi, P., Leonardi, S., and Antonia, R. A., "Turbulent channel flow with either transverse or longitudinal roughness elements on one wall," J. Fluid Mech. **561**, 279–305 (2006).
Perry, A. E., and Chong, M. S., "On the mechanism of wall turbulence," J. Fluid Mech. **119**, 173–217 (1982).
Perry, A. E., and Marusic, I., "A wall-wake model for the turbulence structure of boundary layers. Part 1. Extension of the attached eddy hypothesis," J. Fluid Mech. **298**, 361–388 (1995).
Pirozzoli, S., Bernardini, M., and Orlandi, P., "Large-scale motions and inner/outer layer interactions in turbulent Couette–Poiseuille flows," J. Fluid Mech. **680**, 534–563 (2011).
Raupach, M. R., Antonia, R. A., and Rajagopalan, S., "Rough-wall turbulent boundary layers," Appl. Mech. Rev. **44**, 1–25 (1991).
Rawat, S., Cossu, C., Hwang, Y., and Rincon, F., "On the self-sustained nature of large-scale motions in turbulent Couette flow," J. Fluid Mech. **782**, 515–540 (2015).
Schultz, M. P., and Flack, K. A., "Outer layer similarity in fully rough turbulent boundary layers," Exp. Fluids **38**, 328–340 (2005).
Squire, D. T., Morrill-Winter, C., Hutchins, N., Schultz, M. P., Klewicki, J. C., and Marusic, I., "Comparison of turbulent boundary layers over smooth and rough surfaces up to high Reynolds numbers," J. Fluid Mech. **795**, 210–240 (2016).
Stanislas, M., Perret, L., and Foucaut, J., "Vortical structures in the turbulent boundary layer: A possible route to a universal representation," J. Fluid Mech. **602**, 327–382 (2008).
Tachie, M. F., Bergstrom, D. J., and Balachandar, R., "Roughness effects in low-Re_θ open-channel turbulent boundary layers," Exp. Fluids **35**, 338–346 (2003).
Toh, S., and Itano, T., "Interaction between a large-scale structure and near-wall structures in channel flow," J. Fluid Mech. **524**, 249–262 (2005).
Townsend, A. A., *The Structure of Turbulent Shear Flow*, 2nd ed. (Cambridge University Press, 1976).
Tsukahara, T., Kawamura, H., and Shingai, K., "DNS of turbulent Couette flow with emphasis on the large-scale structure in the core region," J. Turbul. **7**, 1–16 (2006).
Tutkun, M., and George, W. K., "Lumley decomposition of turbulent boundary layer at high Reynolds numbers," Phys. Fluids **29**, 020707 (2017).
Volino, R. J., Schultz, M. P., and Flack, K. A., "Turbulence structure in a boundary layer with two-dimensional roughness," J. Fluid Mech. **635**, 75–101 (2009).
Volino, R. J., Schultz, M. P., and Flack, K. A., "Turbulence structure in boundary layers over periodic two- and three-dimensional roughness," J. Fluid Mech. **676**, 172–190 (2011).
Wu, Y., and Christensen, K. T., "Outer-layer similarity in the presence of a practical rough-wall topography," Phys. Fluids **19**, 085108 (2007).